MODELING ROCK CUTTING USING DEM WITH CRUSHABLE PARTICLES

by

Jorge Alejandro Mendoza Rizo

B.S in Civil Engineering, Universidad Nacional de Colombia, 2008

Submitted to the Graduate Faculty of

Swanson School of Engineering in partial fulfillment

of the requirements for the degree of

Master of Science in Civil Engineering

University of Pittsburgh

2010

UNIVERSITY OF PITTSBURGH

SWANSON SCHOOL OF ENGINEERING

This thesis was presented

by

Jorge Alejandro Mendoza Rizo

It was defended on

April 1st, 2010

and approved by

Jeen-Shang Lin, Sc. D., Associate Professor

Luis E. Vallejo, Ph. D., Professor

John Brigham, Ph. D., Assistant Professor

Thesis Advisor: Jeen-Shang Lin, Sc. D., Associate Professor

iii

MODELING ROCK CUTTING USING DEM WITH CRUSHABLE PARTICLES

Jorge Alejandro Mendoza Rizo, M.S.

University of Pittsburgh, 2010

A numerical model for the rock scratching tests subjected to sharp cutters is proposed in which the rock is represented by a bonded-particle model and its mechanical behavior is simulated by the Distinct-Element Method using the discrete element program PFC2D. The rocks that are modeled represent sandstones and their model micro-parameters are calibrated with laboratory test simulations. The specimen used in the rock scratching test is distinguished by the particle size of a rock sample and the crushability of particles, which affect the failure mode and the cutting force pattern during a scratch test. This study implements a particle crushing criterion that is rooted in micromechanics, and a size-dependent particle strength rule adopted is derived from laboratory results.

The depth of cutting studied is shallow, namely, the cutting depth is no deeper than 1 mm. For this type of shallow cut, ductile failure represents the dominant failure mode. The cutting force recorded during a scratch test fluctuated as a cutter moved through a sample, and this study computes the average force by fitting a straight line to the accumulated mechanical work done by a cutter.

This study demonstrates that both the fragmentation process and the cutter force can be modeled reasonably well. Particularly, this study is able to duplicate an important laboratory result that the specific cutting energy of a shallow scratch test is proportional to the unconfined compression strength of the rock being cut. The potential implications of particle crushing have also been explored.

TABLE OF CONTENTS

LIST OF TABLES

LIST OF FIGURES

ACKNOWLEDGEMENTS

Grateful acknowledgement is given to my advisor, *Dr. Jeen-Shang Lin*, who helped me focus my ideas, and whose intellectual contributions were crucial in the development of this study. My gratitude is also expressed to my committee members, *Dr. Luis E. Vallejo* and *Dr. John C. Brigham*, whose lessons developed my inventiveness and dared me to think beyond the written.

To my *alma mater*, Universidad Nacional de Colombia Sede Manizales, and the professors who showed me the beauty of Civil Engineering.

To my coworkers and friends who joined me in this journey and demonstrated outstanding examples of perseverance and discipline.

To my family; my mother, who teaches me everyday how to be strong-minded; my father, who has been, and always will be, my professor and best friend; and my siblings, who are my role models.

Finally, to my love Luisa, who owns my universe.

1.0   INTRODUCTION

Understanding the mechanics of rock cutting and developing a credible modeling framework has important implications across a diverse field of applications including drilling for oil , mining for coals and minerals, and tunneling and underground cavern construction, just to name a few. From the modeling perspective, rock cutting analysis poses a daunting challenge. Through scratching tests, Richard et al. [1] have reported that rock cutting may evoke different failure modes depending on the depth that a cutter reaches in the rock. How to capture the different failure modes through an analysis without a prior knowledge of which mode would prevail is one of the key issues confronting rock cutting modeling.

To establish the credibility of a modeling technique it is essential that the results are verifiable. The rock cutting as represented by a Rock Scratching Test (RST) represents an excellent way for validation. First of all, it resembles a linear cutting action of a polycrystalline diamond compact (PDC) bit[1]. Furthermore, the test is not only simple in its geometrical and mechanical set up, the failure progression can also be readily be observed both in the failure patterns and force time history. This study therefore focuses on the modeling of rock cutting as a problem posed by a typical RST.

---

[1] **PDC bit:** A drilling tool that uses cutters to shear rock with a continuous scraping motion (Taken from http://www.glossary.oilfield.slb.com/)

1

This research employed the Discrete Element Method [2] (DEM) and the representation of rocks with discrete elements is described first. Then, the rock cutting problem posed by a scratching test is presented. After, considerations of particle crushing implementation are detailed and the implications of particle crushing in rock cutting are explored.

1.1   OBJECTIVES AND SCOPE

The objectives of the present study have a different focus from the ones described in the LITERATURE REVIEW, namely, the goals are to obtain quantitative results. More specifically, the aim is to setup a DEM model so that it is capable of duplicating the horizontal cutter force history and the fragmentation configuration as those obtained from a physical test. Richard [3] has performed a series of rock scratching tests which this study attempted to model. His experiments showed that during a shallow cut, where the depth of the cutter into the rock was no more than 1mm, the rock failed in a ductile mode. In a ductile failure mode, the cutter force resembles that of an elasto-plastic material under yield. Whereas during a deeper cut, the failure resembles that of a brittle failure and often a crack is created, progresses and is finally forced into a chip with corresponding cutter force exhibited cycles of rising up and coming down.

2.0   LITERATURE AND METHODOLOGY REVIEW

The literature review is focused narrowly on the applications of DEM to rock cutting. A brief review of the DEM formulation as adopted the Particle Flow Code (PFC) and the contact model used for modeling rock are first presented. Then, a basic description of the scratching test characteristics are reviewed for the specific case of a sharp cutter and a shallow cut. The available literature is then discussed.

2.1   DISTINCT ELEMENT METHOD IN PFC

2.1.1   Distinct Element Method

The Distinct Element Method (DEM) is a specific application of a broad numerical method named the Discrete Element Method. The Distinct Element Method was first laid out by Cundall [4] for rock mechanics analysis and subsequently applied to soil mechanics problems by Cundall and Strack [2]. In this Discrete Element Method, each discrete element, or particle, has three degrees of freedom in a two dimensional setting, namely, two translational and one rotational. At each time step a rigid body dynamics equation is solved for each particle. The interaction between particles is implemented through the penalty method in which very stiff springs are used

to both prevent excessive particle overlap, and to enable the computation of forces between particles.

The solution method used for solving a particle system is based on the explicit finite-difference method . The explicit method scheme requires the use of very small time step size for stability and accuracy, but avoids the need to solve simultaneous equation.

The timestepping algorithm assumes that both the velocity and acceleration are constant inside the time step. The maximum timestep that can be used is dictated by the fundamental period of the system. Because of the high stiffness used, the time step is very small often in the order of 10^{-9} seconds.

At each time step, the equation of motion is solved for each particle. The forcing term comes from external loads as well as from interaction with neighboring particles. The interaction forces, or contact forces, are updated using the force-displacement law from the relative motion at each contact.

2.1.2   Contact model

In the 2D DEM, in addition to circular particles, which are also referred to as balls, are rigid walls that are employed to impose displacement constraints. Accordingly, two types of contacts are encountered, i.e., ball-ball and ball-wall. A contact model dictates how a contact behaves by defining the follow characteristics: 1) stiffness, which relates the relative displacements to the contact force; 2) slip, which provides a relation between normal and shear forces; 3) damping, which dissipates kinetic energy in order to achieve a steady-state; and 4) bonding, which allows particles to be bonded for transferring forces only, e.g., contact bond, or both forces and

moments, e.g., parallel bond. There are two types of bond: (1) contact bonds, which can transfer force only; and (2) parallel bonds, which can transfer both forces and moments.

The linear stiffness model is the simplest model in which the stiffness maintains a constant value until a failure takes place. Figure 2.1depicts a linear normal contact on the left and a linear shear contact on the right. The normal contact will be removed when particle loses contacts, or the spring is subjected to net tensile force. A shear spring fails, as represented by a slider, when its strength, often defined by the Mohr-Coulomb law, is exceeded.

http://nptlab.tistory.com
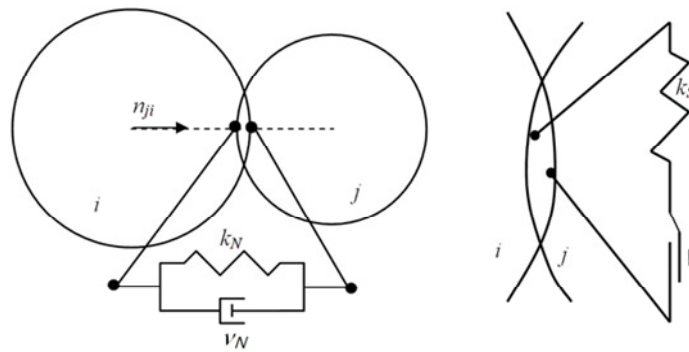
Figure 2.1 Linear model implementing stiffness, slip, and damping at contact

To model a rock sample in DEM, in this study, the rock is modeled by the Bond-Particle Model (BPM) of Potyondy and Cundall [5], in which particles are cemented together with bonds. First, an assembly of circular particles is created following a particular grain size distribution. This assembly is then packed under a preset level of compressive stress and bonded together at the points of contact between particles. The particular type of bond used is called the parallel bond which can be visualized as a finite-sized piece, or in our case a cylinder (depicted in Figure 2.2) of cementitious material with its diameter proportional to the minimum diameter of the two particles that a bond cements.

5
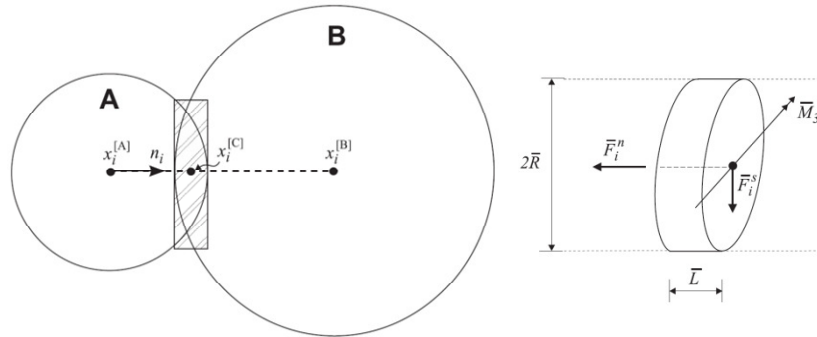
Figure 2.2 Parallel bond visualization as a cylinder of cementitious material [6]

When the bonds are in place, particles are not allowed to slide. Only after the bonds are broken, such as the creation of cracks, sliding is considered. The cementitious material can be visualized as well as a set of uniformly distributed springs over this region. The spring forces and moments can be related to maximum stresses acting within the bond periphery, and a bond can be broken when the strength is exceeded by the maximum stresses.

2.2   SYNOPSIS OF THE ROCK SCRATCHING TEST

The Rock Scratching Test (RST) will be the basis for validating the modeling effort of this study. In this test, the cutter moves in a linear fashion into a rock sample. The thinking here is that there is no sense in attempting to model sophisticated drilling bit action, unless this much simpler problem can be tackled in a satisfactory manner. the following section explains briefly the RST scheme, and how it has been modeled so far.

2.2.1 The Rock Scratching Test as a technique

In the oil industry, or any other industry which requires that a natural resource be extracted, drilling is one of the most critical and expensive stages of an oil extracting project. However, the phenomenon of well drilling lacks a strong theoretical approach with respect to the interaction between the rock and drag bit. The Rock Scratching Test (RST) is a laboratory test performed over either a slab or a cylinder obtained from a rock core. The rock specimen is scratched in a single direction throughout the sample, using a cutting tool which mimics one of the tips of a drill bit, or drag bit, used for well drilling [7]. Purposes of the RST are: 1) to register the horizontal force acting on the cutting tool and 2) to observe the failure behavior of the rock. Hence, the Uniaxial Compressive Strength (UCS) can be well estimated based on the cutting mechanism observed in the experiment, and the forces acting on the cutting face [1, 3].

Based on experimental observation, Richard [3] concluded that two cutting modes in the rock cutting process take place in the RST: 1) a "ductile" failure mode occurring at shallow depths (generally less than 1mm) is associated with crushing of particles at the tool tip and shearing of the rock in front the cutter; and 2) a brittle mode occurring at greater depths (generally more than 1 mm), characterized by macroscopic cracks that initiate from the tip of the cutter creating uneven paths of failure ahead of the cutter. The two types of failure modes are depicted in Figure 2.3.

(a) **(b)**

Figure 2.3 The Rock Scratching Test: (a) a ductile failure mode and (b) a brittle failure mode

It was found in the shallow cutting process that the Uniaxial strength is related to the specific energy of cutting. The latter is defined by the author as the energy required to cut a unit volume of rock. Equation 2.1 presents the relation between the specific, ε, and the mean horizontal force on a shallow cutting, F_S, here w and d respectively stands for the width of the cross-sectional scratched section and the depth of cutting.

$$\varepsilon = \frac{F_S}{wd}$$

Equation 2.1

The Rock Strength Device (RSD) is used to perform the RST. The size of the rock sample (cores) that can be used in the RSD ranges from 30 *mm* to 120 *mm* in diameter, and 20 *mm* to 1000 *mm* in length according to Schei et al. [8]. In addition, the length of the groove scratched has to be at least 10 times the depth of the cutting. Thus, a sample subjected to shallow

cutting can offer good results after 10 *mm* of a cutting process. A more detailed description of the apparatus and the configuration of the test was presented by Richard [3].

2.2.2   Discrete Element Modeling of RST

In general, the DEM modeling of rock cutting has been performed taking into account the following conditions: 1) The rock is modeled as a BPM, 2) the walls containing the specimen are boundary conditions at zero velocity, and 3) the cutting tool is a segmented wall, representing a boundary condition at a constant velocity. The nature of the rock being a BPM and the cutting tool a rigid body, allows for identification of the damage in the bulk material and the recording of the forces acting in the cutting process, respectively.

The different failure modes in rock cutting was modeled by Huang et al. [9]. They found that the depth of cutting determines whether the failure regime is ductile or brittle when a characteristic particle size is given. The authors also found a fair relationship between specific energy of cutting and the unconfined compressive strength of the sample.

Lei et al. [10, 11] has explored the use of DEM in modeling rock scratching tests by performing studies on the influence of hydrostatic pressure on orthogonal machining and sensitivity analyses of the micro-properties of the numerical model. The specimen particle distribution and boundary conditions setup are shown in Figure 2.4. The authors suggest that the increment of particle size towards the bottom of the sample decreases the computational expenses without affecting the macro-properties of the material. The findings in these studies are that: 1) the hydrostatic effect restrains crack growth and creates larger horizontal forces during the cutting process, 2) the failure in the absence of confining pressure implies short-chip formation, crack propagation and smaller cutting forces 3) the damping coefficient has a large

9

effect in the cutting forces, therefore a more realistic value is necessary for having closely results to reality, and 4) the shape of the particles for avoiding the spinning that the circular elements allows also affects the results, suggesting further research in the implementation of clusters in the specimen.
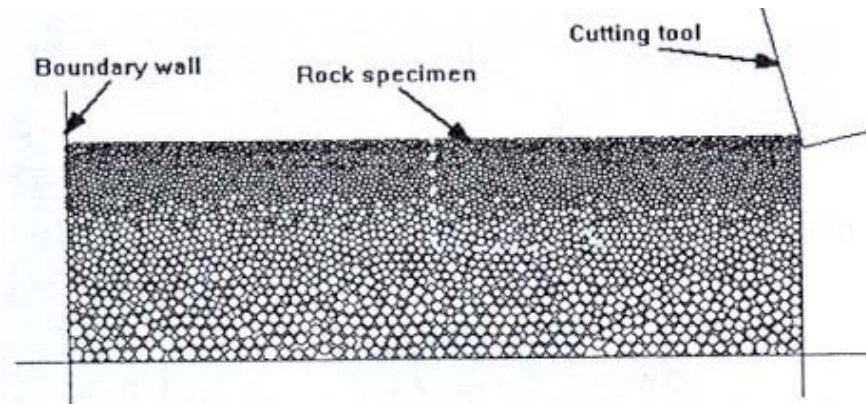
Figure 2.4 Specimen setup and boundaries for rock cutting **[10]**

DEM has been used as well by Rojek [12] in rock cutting simulation with the purpose of validating the cutting force results with the existing analytical approaches of Nishimatsu [13] and Evans [14]. However, this study does not specifically refer to the scratching test nor the shallow cut. Moreover, the study shows an interesting failure pattern that characterizes a deep cutting depth as shown in Figure 2.5.
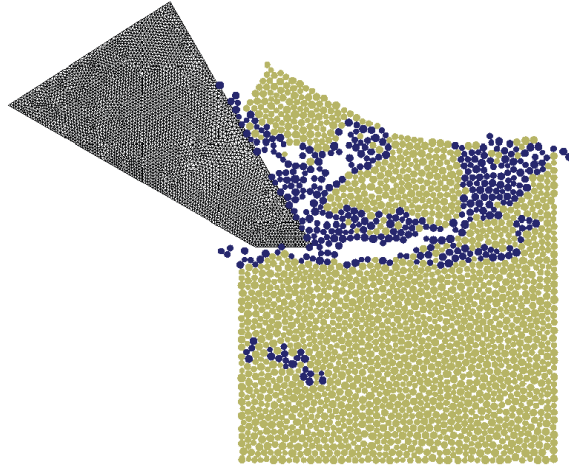
Figure 2.5 Brittle failure in rock cutting **[12]**

Huang and Detournay [15] investigated that the switch from ductile to brittle failure mechanisms can be explained by the introduction of a length scale parameter in the rock description, which is a function of the material toughness and the uniaxial strength. The investigators claim that the mean radius loses its quality of discretization parameter and becomes dependent on the toughness and the uniaxial strength. Thus, when the length scale is introduced, the failure behavior is controlled by the strength of the mechanical properties of the material.

(a)   **(b)**
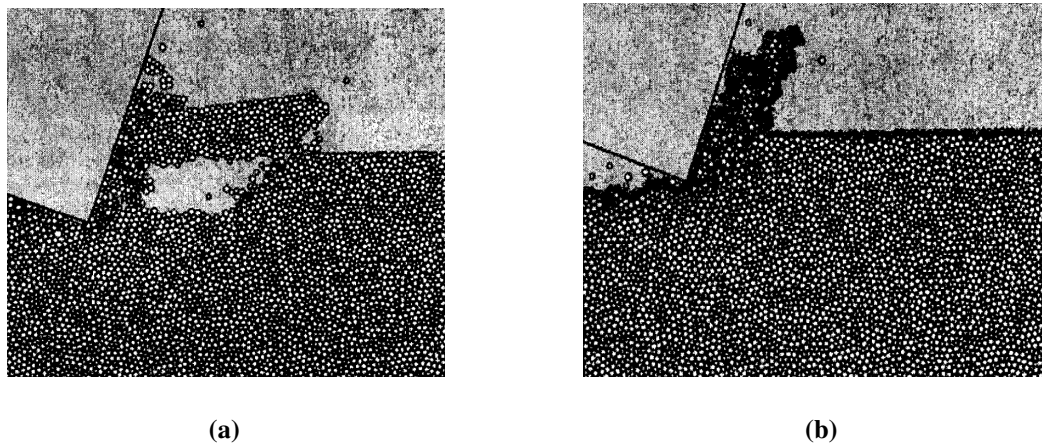
Figure 2.6 Visualization of cutting morphology using DEM at (a) atmospheric conditions and (b) down-

hole conditions

11

Finally, the relation between failure mode in drilling and bottom hole pressure was investigated by Block and Jin [16] using DEM. Here, the energy dissipation was addressed not just as the breaking of the bonds, but also the irreversible reorganization of the grain structure. This issue was accounted for, calculating the average stress tensor and the strain rate on a grain within a given neighborhood. A cap-like failure envelope was considered in the post-processing of the results to determine whether the state of stresses on analyzed regions were behaving elastically, or failing either in a brittle or ductile manner. Moreover, it was found that the cutting morphology is affected by the *in situ* pressure conditions and the weight of the PDC bit, where the case of atmospheric conditions is shown in Figure 2.6(a) while the case of down-hole conditions is shown in Figure 2.6(b).

3.0   DISCRETE ELEMENT SIMULATION

General test setup and the material property selection are described in this chapter. The calibration of the material through different laboratory tests, the aim in choosing these materials, and a brief description of the crushing criterion scheme and its implementation in the numerical model are explained.

3.1   GEOMETRICAL CHARACTERISTICS OF THE SYSTEM

The first issue confronts a modeling effort is how long should a sample be. Richard [3] found that for obtaining stable results, the length to be scratched, or distance of cutting, has to be at least ten times the depth of cutting, e.g., for our case of up to a 1.0 *mm* depth cut, a length of cutting of 10 *mm* is required, otherwise the results might not converge. Because our study is focus only on shallow cuts, we expect cracks, if created, would be shallow as well. This makes it possible to analyze a cutting consider only partial depth of a sample.

Based on these facts, both height (or diameter) and length can be estimated in obtaining a conservative system size that can yield accurate results at a reasonable computational cost. For instance, if a rock sample with a height of 30 *mm* and a length of 50 *mm* was used in a laboratory test, the numerical sample dimensions can be greatly reduced, hence, reducing the computational expenses. In this study, we considered that a numerical sample with 10 *mm* of height and 25 *mm*

of length is sufficient to capture a ductile failure mode and can be scratched up to a distance of 15 *mm* without being affected by any boundary condition of the model. A sketch of the model proposed with respect to the laboratory sample is depicted in Figure 3.1.

Dimensions are in millimeters
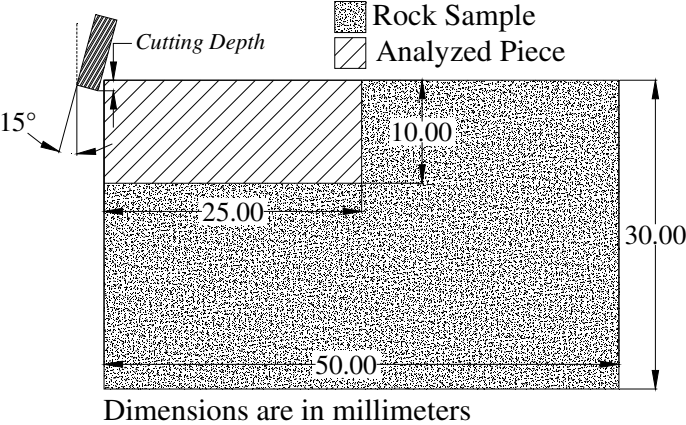
Figure 3.1 Dimension difference between the numerical model and laboratory sample

From the analysis sample shown in Figure 3.1, and taking into account the failure mode that takes place in the shallow scratching test, a region with particles as fine as the real size of the grains in a Vosges sandstone is assigned in the top half of the sample. These particles are distributed in the range from 0.1 *mm* to 0.4 *mm* of diametric size. To reduce the computational cost, the particles size were increased gradually with depth from the bottom half . The top region of the particles is called hereafter the *Cutting Region* as shown in Figure 3.2.

14

Dimensions are in millimeters
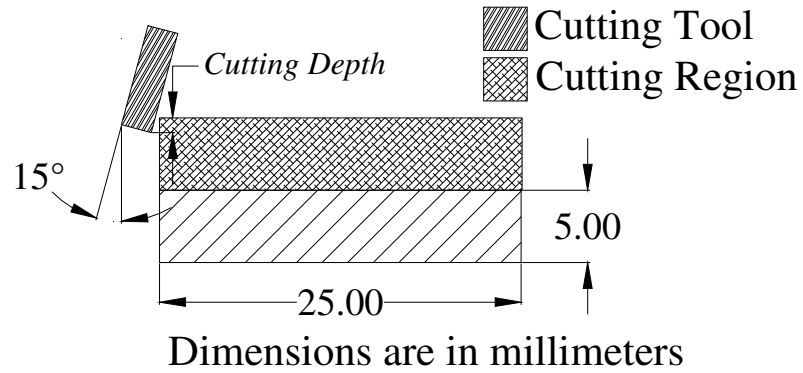
Figure 3.2 Piece of material analyzed numerically

In order to create a numerical specimen with these features in the PFC2D, a refinement function embedded in the code is implemented in different regions assigned throughout the system. A snapshot of the numerical sample is shown in Figure 3.3 where the particle size distribution can be observed. A more detailed explanation about how the specimen was generated can be found in the section Sample preparation.

Lastly, the rake angle of the cutting tool in the model is set to be the same as that used in experiment [3], 15° as depicted in both Figure 3.1 and Figure 3.2.
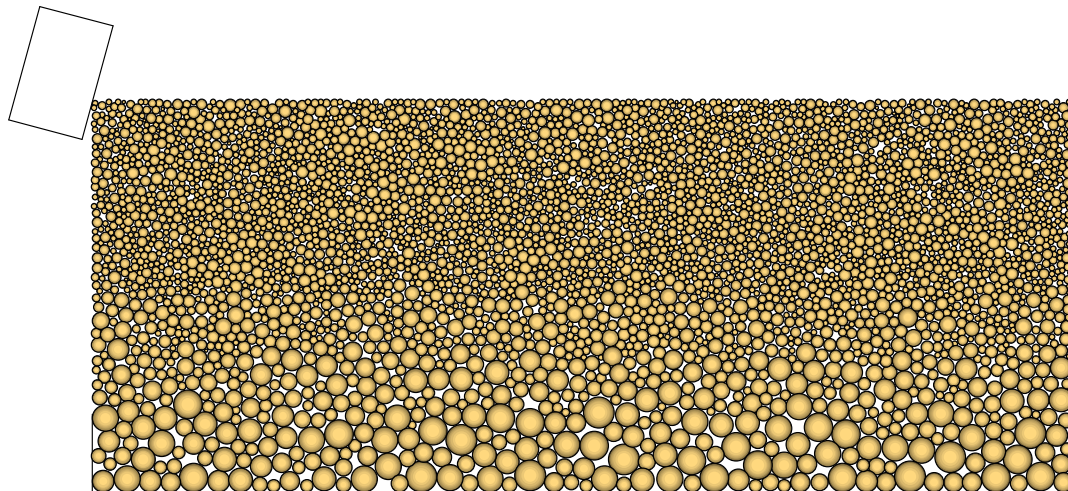
Figure 3.3 Particle size distribution of the DEM model

3.2   CALIBRATION OF THE MATERIAL

Because the scratch test data available are mostly from sandstones [3], and because of the lacking of specific information about the particular rocks used we attempted herein to generate "general" sandstone. Namely, instead of modeling a sandstone that is typically found in a certain region, i.e., Vosges sandstone, Berea Sandstone, among others, we generated sandstone-like material.

In order to achieve this , we used the engineering classification of intact rocks by Deere and Miller [17] as a guide, in which rock can be classified by its Uniaxial Compressive Strength (UCS) and the Young's Modulus at 50% of the UCS. A green dash on the graph in Figure highlights the area corresponding to sandstones while the slopes in red stand as limit indicators for the ratios of Young's Modulus to UCS. Now, our purpose is to generate materials in DEM within the sandstone region.
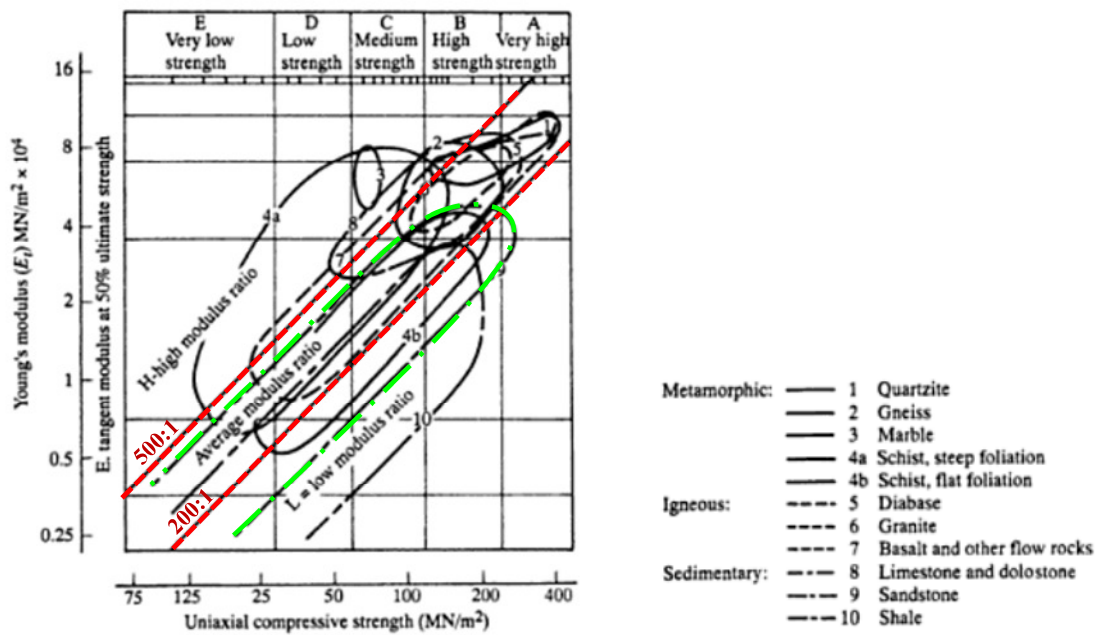
Figure 3.4 Deere and Miller's engineering classification of rocks taken from Bell [18]

16

3.2.1   Laboratory tests

In the scratch test, we used the actual particle size of a sandstone sample. This is not necessary for numerical modeling of laboratory mechanical test. Potyondy and Cundall [5] found that in a PFC2D model, the elastic response of the materials, i.e., Young's Modulus and Poisson Ratio and the unconfined compressive strength, does not seem to be affected by the particle size . Thus, our particle size used in modeling laboratory tests was selected with the computational cost in mind. Potyondy and Cundall [5] chose for the finest particle system an average diameter of 0.36 mm in a rectangular specimen of $63.4 \times 31.7 \, mm^2$, our laboratory test sample used an average diameter of 0.52 mm in a rectangular sample of $100 \times 50 \, mm^2$. The height to width ratio of the sample is kept to 2 to 1.

(a)   (b)
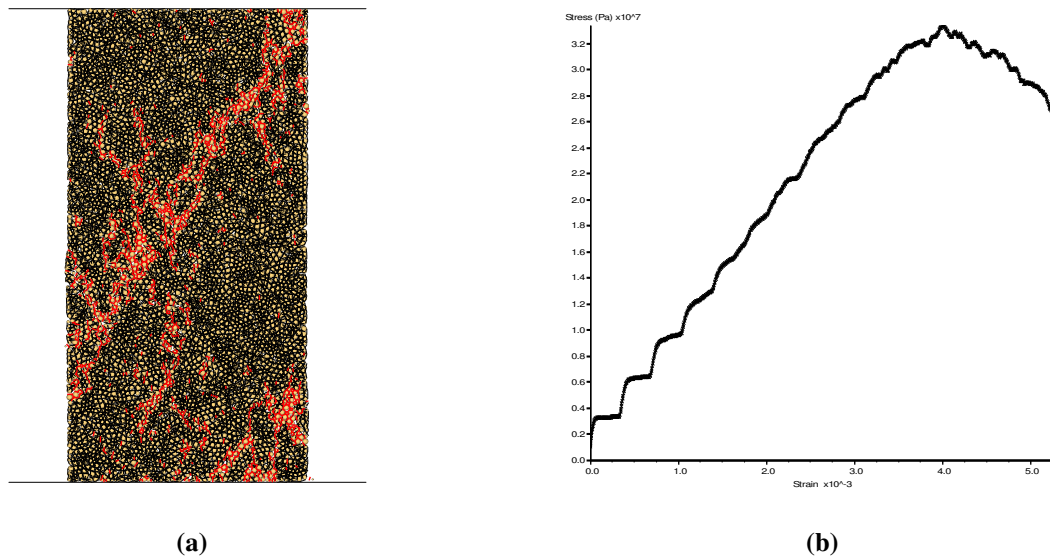
Figure 3.5 Typical Uniaxial Test in PFC2D, where (a) is the sample at failure and (b) is its respective

stress-strain curve

17

Figure 3.5 shows a typical result of a Uniaxial Compressive Test we obtained in PFC2D. A close look reveals that the red and magenta lines in Figure 3.5(a) denote the broken bonds that failed in tension and shear respectively, which mimics the failure of surfaces and cracks on a real rock. The parallel bonds that are intact are represented by parallel black lines while the particles are depicted as light-orange circles in the background. Lastly, the stress-strain curve obtained is plotted in Figure 3.5(b).

(a)   **(b)**
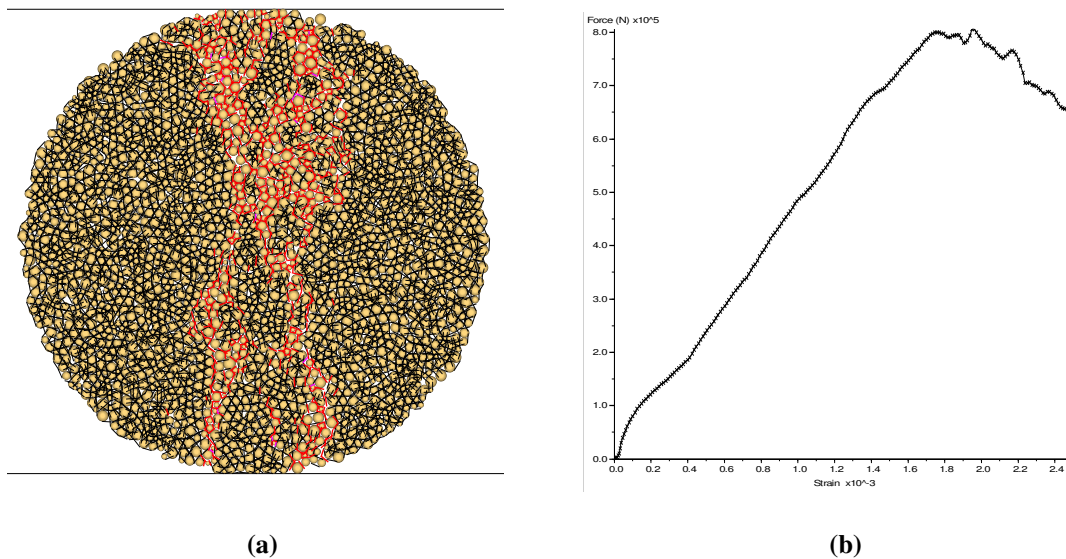
Figure 3.6 Typical Brazilian test in PFC2D, where (a) is the sample at failure and (b) is its respective Force-strain curve

Indirect tensile tests, i.e., the Brazilian tests, were also carried out The failed sample configuration of this test is shown in Figure 3.6(a) and the force-strain curve is plotted in Figure 3.6(b). Both were found to show trend similar to actual tests.

$$t_{crit} = \sqrt{m/k}$$

Equation 3.1

18

An important issue to address in our calibration is that mass scaling was implemented such that the mechanical timestep can be increased during the modeling of the laboratory tests. Because the critical time step [19], t_{crit} in Equation 3.1, is proportional to the square root of the mass, an increase in the mass, i.e., the so-called mass scaling, increased the critical time step and shortened the computational time. The effects of mass scaling by increasing the mass density of balls show rather small impact on the results of numerical test results as summarized in Table 3.1. These results obtained for each density are an average of tests performed on three different assemblies. Through the 1000 times increase in the mass, the computational time was cut by a factor of 31. This significant time saving at the expanse of small loss in resolution is deemed a good trade off.

Table 3.1 Mass scaling influence on the Young's Modulus and the Unconfined Compressive Strength

ρ (kg/cm^3)	σ_c (MPa)	E (GPa)
2630	66.70	5.56
2'630,000	70.10	5.67
Difference	5.10%	1.98%

3.2.1.1 Micro-parameter selection

The numerical model requires a set of micro-parameters to create a BPM. These micro-parameters refer to the properties of the constitutive model in general, where the particles and their contacts are involved.

A large number of DEM rock mechanical tests were conducted, e.g., Unconfined Compressive Strength (UCS) and Brazilian Tests, to ensure that the selected micro-parameters yielded reasonable rock samples. How changes in these parameters could impact macro-

properties of rocks were studied, and the results are summarized herein. Even though the parallel bonds were employed to cement grain particles into rock, an exploration using contact bonds was also included. The results of this sensitivity study provided a guide for the selection of the micro-parameters and its influence on the macro-properties. For instance, when we needed to increase the uniaxial strength of the rock, the sensitivity study results gave a guideline or parameters in which to change and by how much.

The sensitivity study reached the following conclusions:

- The unconfined compressive and tensile strengths are proportional to the bond strength as shown in Figure 3.7(a) and Figure 3.7 (b), respectively

- The Young's Moduli and Poisson Ratios increase with the normal stiffness of both particle bonds as depicted in Figure 3.8(a) and Figure 3.8 (b), respectively. These are also affected by the type of bonding. For instance, in Figure 3.9(a) it is shown that the contact bond does not affect either, but the parallel bond affects proportionally the Poisson Ratio shown in Figure 3.9(a).

- The Young's Modulus shows a strong proportionality in both of the bonding models as can be observed in Figure 3.10. However, it is important to notice that the results obtained using the contact bond model, Figure 3.10(a), are less stable than the ones obtained using the parallel bond model, Figure 3.10(b).

This sensitivity analysis was not extensive and had a narrow focus of assisting in obtaining micro-parameters quickly.
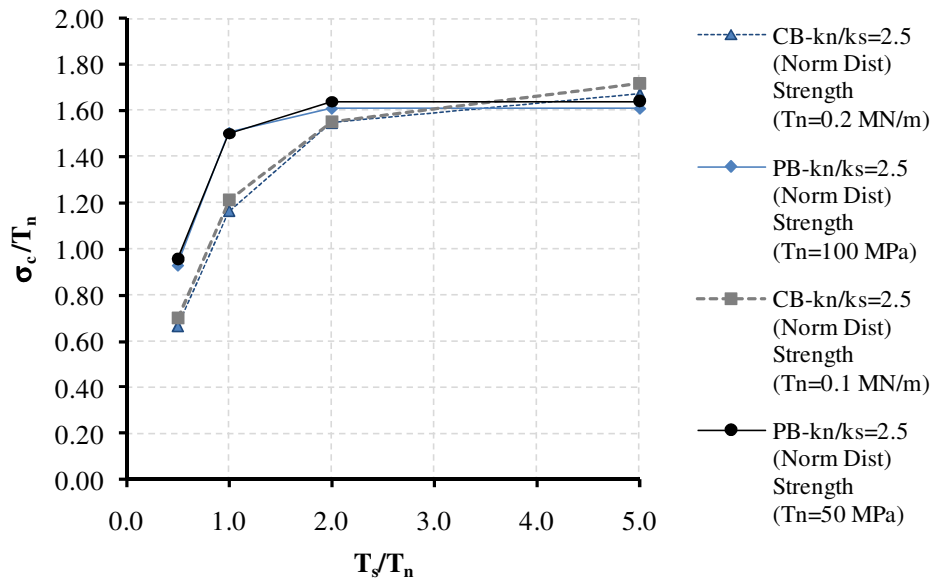
(a)
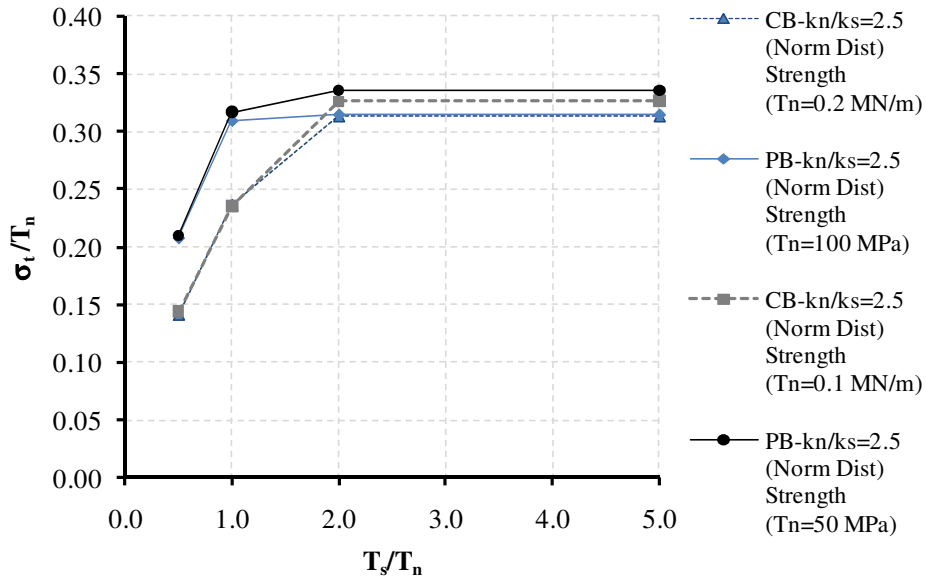
(b)

Figure 3.7 Bond strength influence on: **(a)** Unconfined Compressive Strength and **(b)** Tensile Strength
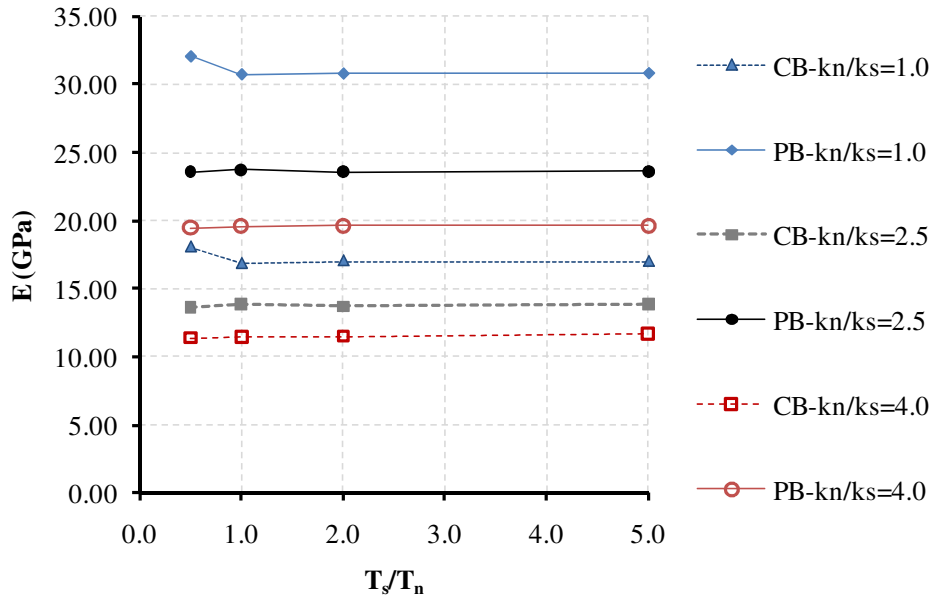
(a)
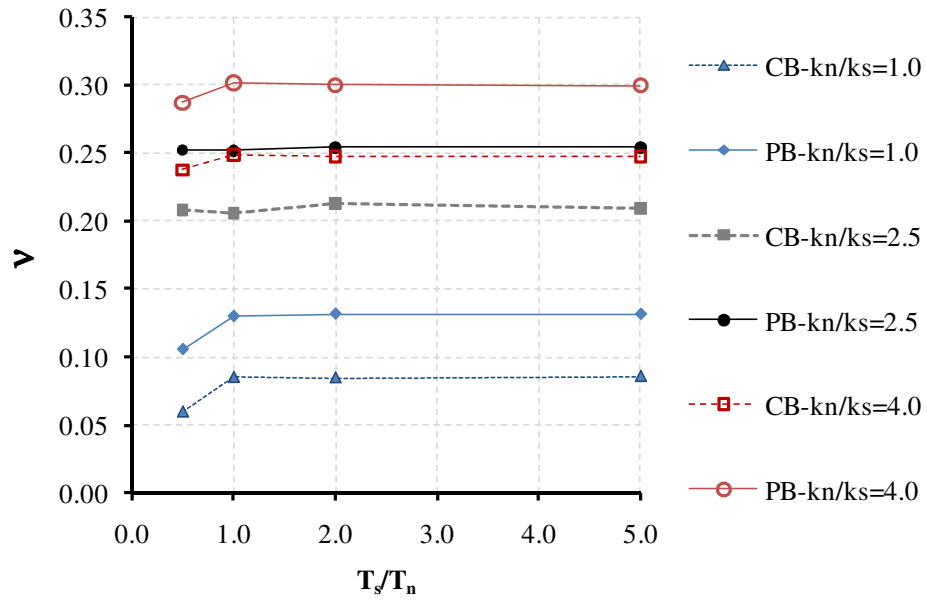
(b)

Figure 3.8 Normal stiffness of particles and bonds affecting **(a)** the Young's Modulus and **(b)** the Poisson

Ratio
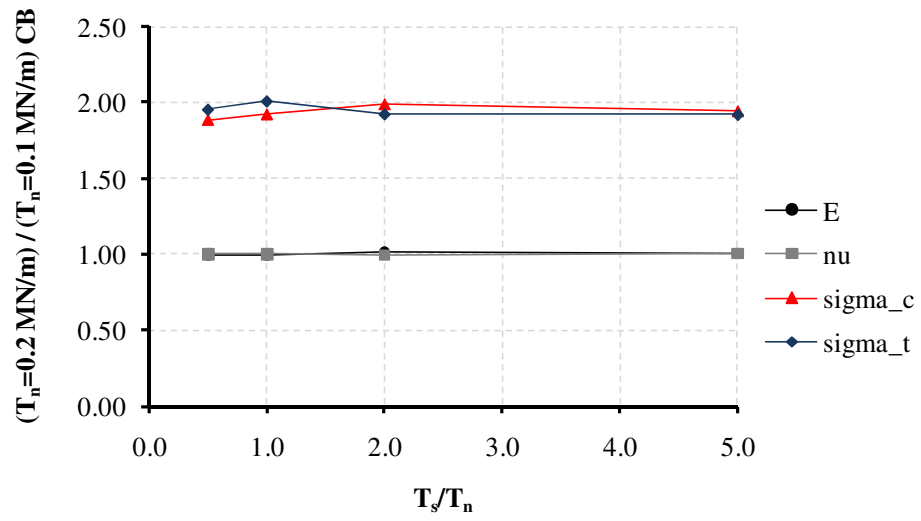
(a)
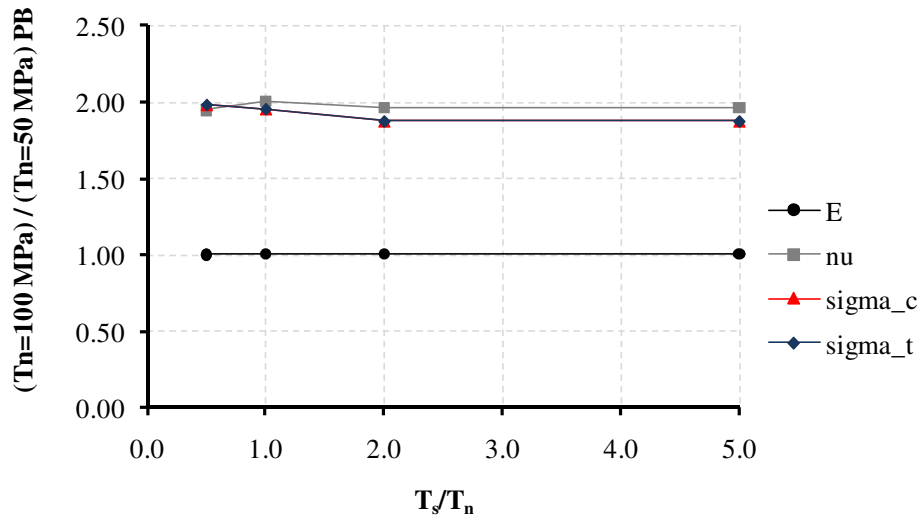
(b)

Figure 3.9 Influence of macro-properties due to bond strength on **(a)** the contact bond model and **(b)** the

parallel bond model
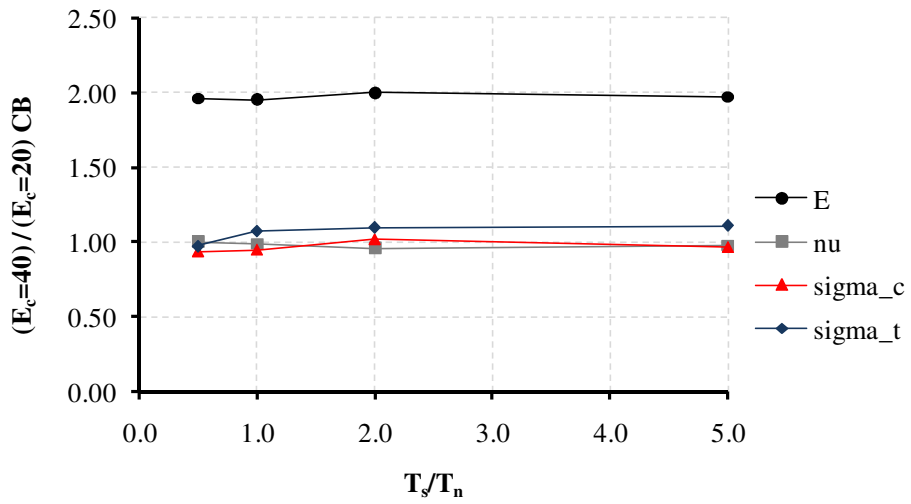
(a)
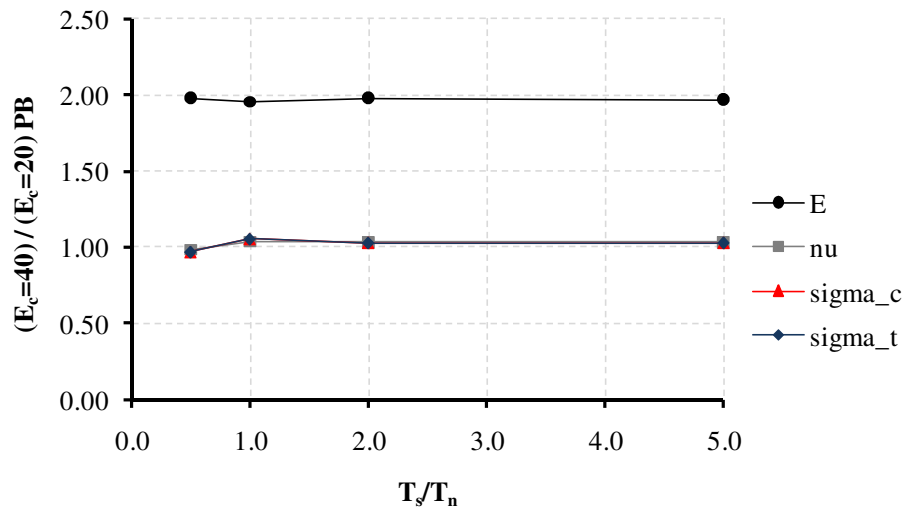
(b)

Figure 3.10 Macro-properties affected by the Young's Modulus on **(a)** the contact bond model and **(b)** the

parallel bond model

3.2.2 Cases of sandstones modeled

In creating a general set of samples that are typical of sandstones, two groups of sandstones were created based on two different Young's Modulus to ultimate strength ratios represented by the red lines in Figure 3.4.

The first set of four samples created is named CASE I, and the micro-properties for this case are shown in Table 3.2. Here, each sample material is differentiated by a set of three parameters: the Young's Modulus of both the particle and the bond, and the normal strength of the bond. The rest of the parameters are kept the same. For instance, the material *SS_25_I* denotes a sandstone, for *SS*, with a mean bond normal strength of 25 *MPa* in CASE I. The corresponding particle Young's Modulus was 3 *GPa*, and the Young's Modulus of the bond was also 3 *GPa.* Moreover, all these three parameters are marked as material (*i*). Similarly, *SS_50_I* would have a mean bond normal strength of 50 *MPa*, and both bond and particle Young's Modulus are equal to 6 GPa. These parameters are marked as material (*ii*)

Table 3.2 PFC2D micro-properties for CASE I

GRAINS (PARTICLES)	CEMENT (PARALLEL BONDS)
$\rho = 2630\ kg/m^3$ $E_c = \begin{cases} (i)\ 3\ GPa \\ (ii)\ 6\ GPa \\ (iii)\ 9\ GPa \\ (iv)\ 12\ GPa \end{cases}$ $R_{max}/R_{min} = 1.66$ $R_{min} = 0.3 \times 10^{-3}\ m$ $k_n/k_s = 1\ \therefore\ k_n = 2tE_c\ ,\ t = 1$ $\mu = 0.5$ Where, ρ : Density R_{max}, R_{min} : Maximum and minimum radius, respectively E_c : Young's Modulus k_n : Normal Stiffness k_s : Shear Stiffness μ : Friction	$\bar{\lambda} = 1$ $\bar{R} = \bar{\lambda} \times min(R^{(A)}, R^{(B)})$ $\bar{E}_c = \begin{cases} (i)\ 3\ GPa \\ (ii)\ 6\ GPa \\ (iii)\ 9\ GPa \\ (iv)\ 12\ GPa \end{cases}$ $\bar{k}^n/\bar{k}^s = 1\ \therefore\ \bar{k}^n = \bar{E}_c/(R^{(A)} + R^{(B)})$ $\bar{\sigma}_c = 0.5\bar{\tau}_c = (mean \pm std.dev.)$ $\therefore\ mean = \begin{cases} (i)\ 25\ MPa \\ (ii)\ 50\ MPa \\ (iii)\ 75\ MPa \\ (iv)\ 100\ MPa \end{cases}\ ;\ std.dev. = 23\%$ Where, $\bar{\lambda}$: Bond Radius Multiplier $\bar{R}$: Bond Radius $R^{(A)}, R^{(B)}$: Radius of particle in contact A and B, respectively $\bar{E}_c$: Young's Modulus $\bar{k}^n$: Normal Stiffnes $\bar{k}^s$: Shear Stiffnes $\bar{\sigma}_c$: Normal Strength $\bar{\tau}_c$: Shear Strength

Each set of material parameters was used in creating three different samples. The samples were different because particles were geneated and placed randomly. The average results of Uniaxial and Brazilian tests on the set of CASE I materials are provided in Table 3.2.

Table 3.3 Summary results of Uniaxial and Brazilian tests from CASE I materials

Summary	σ_c (MPa)	ν	E (GPa)	σ_t (MPa)	E/σ_c
Sample with 25 *MPa* of normal parallel bond (*SS-25_I*)	_29.95_	0.15	_4.87_	6.23	_162.48_
Sample with 50 *MPa* of normal parallel bond (*SS-50_I*)	_67.65_	0.17	_9.27_	11.28	_137.09_
Sample with 75 *MPa* of normal parallel bond (*SS-75_I*)	_88.41_	0.17	_13.76_	17.85	_155.62_
Sample with 100 *MPa* of normal parallel bond (*SS-100_I*)	_121.42_	0.17	_18.17_	25.85	_149.66_

The same philosophy is adopted for creating four materials denoted as CASE II. The parameters and the results of the laboratory tests on them are summarized in Table 3.4 and in Table 3.5, respectively.

Table 3.4 PFC2D microproperties for CASE II

GRAINS (PARTICLES)	CEMENT (PARALLEL BONDS)
$\rho = 2630 \ kg/m^3$ $E_c = \begin{cases} (i) \ 6 \ GPa \\ (ii) \ 12 \ GPa \\ (iii) \ 18 \ GPa \\ (iv) \ 24 \ GPa \end{cases}$ $R_{max}/R_{min} = 1.66$ $R_{min} = 0.3 \times 10^{-3} \ m$ $k_n/k_s = 1 \ \therefore \ k_n = 2tE_c \ , t = 1$ $\mu = 0.5$ Where, ρ : Density R_{max} , R_{min} : Maximum and minimum radius, respectively E_c : Young'sModulus k_n : Normal Stiffness k_s : Shear Stiffness μ : Friction	$\bar{\lambda} = 1$ $\bar{R} = \bar{\lambda} \times min(R^{(A)}, R^{(B)})$ $\bar{E}_c = \begin{cases} (i) \ 6 \ GPa \\ (ii) \ 12 \ GPa \\ (iii) \ 18 \ GPa \\ (iv) \ 24 \ GPa \end{cases}$ $\bar{k}^n/\bar{k}^s = 1 \ \therefore \ \bar{k}^n = \bar{E}_c/(R^{(A)} + R^{(B)})$ $\bar{\sigma}_c = 0.5\bar{\tau}_c = (mean \pm std.dev.)$ $\therefore \ mean = \begin{cases} (i) \ 25 \ MPa \\ (ii) \ 50 \ MPa \\ (iii) \ 75 \ MPa \\ (iv) \ 100 \ MPa \end{cases} ; \ std.dev. = 23\%$ Where, $\bar{\lambda}$: Bond Radius Multiplier $\bar{R}$: Bond Radius $R^{(A)}, R^{(B)}$: Radius of particle in contact A and B, respectively $\bar{E}_c$: Young's Modulus $\bar{k}^n$: Normal Stiffnes $\bar{k}^s$: Shear Stiffnes $\bar{\sigma}_c$: Normal Strength $\bar{\tau}_c$: Shear Strength

Table 3.5 Summary results of Uniaxial and Brazilian tests from CASE II materials

Summary	σ_c (MPa)	ν	E (GPa)	σ_t (MPa)	E/σ_c
Sample with 25 MPa of normal parallel bond (SS-25_II):	35.31	0.15	9.46	8.61	268.03
Sample with 50 MPa of normal parallel bond (SS-50_II):	79.96	0.16	18.25	14.09	228.20
Sample with 75 MPa of normal parallel bond (SS-75_II):	97.85	0.16	27.32	23.31	279.18
Sample with 100 MPa of normal parallel bond (SS-100_II):	129.78	0.17	35.91	30.91	276.73

Marking the results using the data from Table 3.4 and Table 3.5 into the classification chart of Figure 3.11, the actual classifications of generated materials are found to be within the range of sandstones targeted.
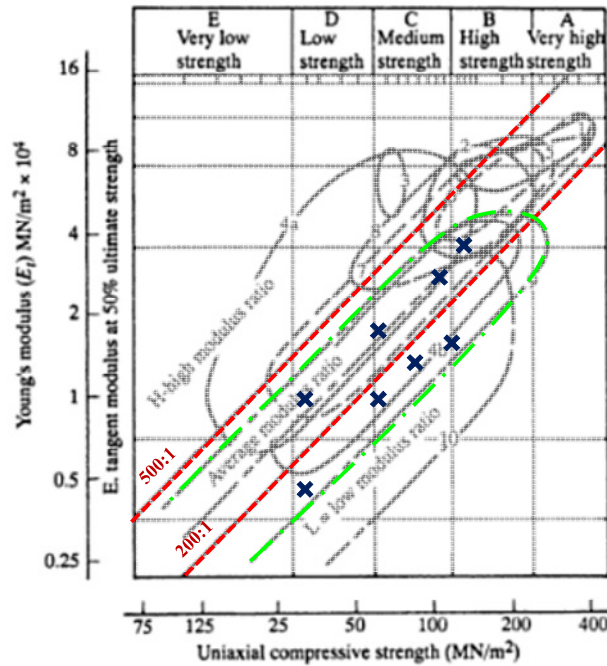
Figure 3.11 Engineering classification of rocks with materials generated marked on.

3.3   PARTICLE CRUSHING

Particle crushing is implemented as follows: First, if the induced tensile stress on the particle exceeds its strength, a particle will be crushed; Secondly, when it is crushed, a particle is replaced by a number of smaller particles without bonds; and if the particle is bonded to others, these bonds are deleted. Finally, the post crushing configuration and the number of the particles

formed as proposed by Tsuongui et al. [20] were adopted. However, the conservation of mass criterion proposed by Åström [21] was not implemented because of the losing-mass nature of the test due to the scratching.

The average stress within a rigid particle can be defined in terms of the peripheral forces and their position vector as shown below,

$$\overline{\sigma}_{ij} = \frac{1}{V_p} \sum_{c=1}^{n} r_i^c F_j^c$$

Equation 3.2

where, V_p is the volume of a particle, F is one of the n contact forces acting on the particle, and r is a position vector measured from the center of the particle to the contact force point [22].

3.3.1 Determination of a particle crushing strength

A theoretical model for failure criterion on a particle in the DEM developed by Tsuongui et al. [20] was implemented in this study, where an arbitrary system of contact forces is considered for calculating the average state of stresses on each particle, and from there, two principal states of stresses, the hydrostatic and the deviatoric, are converted to two pairs of loads forming an inclined cross as sketched in Figure 3.12. These pair of loads then are used in computing the maximum tensile stress in the center of the particle, thus, in determining if the particle would be cracked or crushed. The rational for this step was based upon the finite element results that

29

Tsuongui et al. obtained in which fracture was found not originated at contacts but in the center of the particle.

(a)

(b)
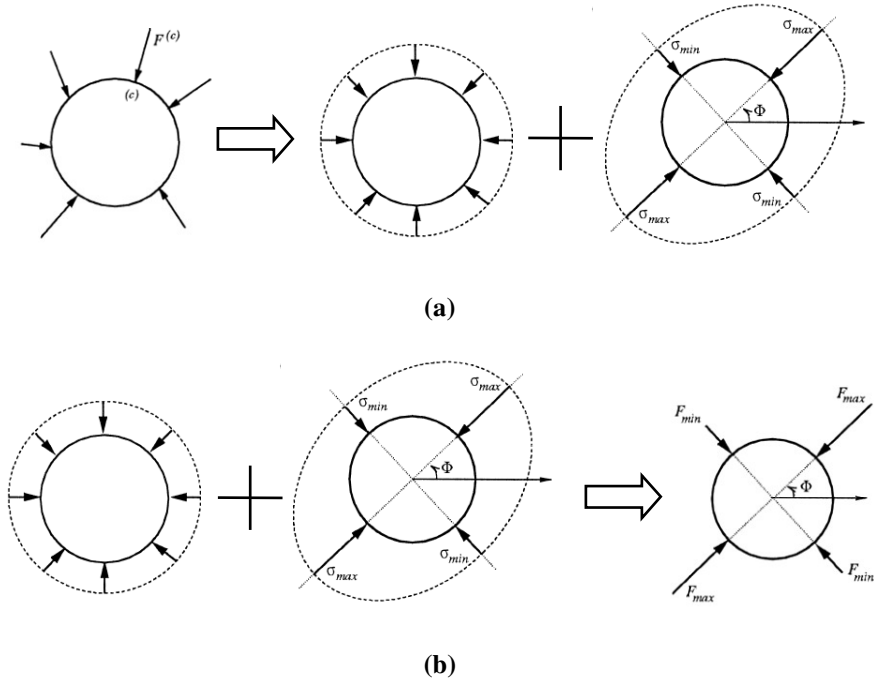
Figure 3.12 Correspondence between (a) contact forces and principal state of stresses in a particle; and between (b) principal state of stresses and two couple of loads forming an inclined cross [20].

3.3.2 Determination of a particle crushing strength

After the stresses that cause failure are found, the strength of the particle with respect to crushing is the next step in the process. It is known that the particle crushing strength is particle size dependent with high variability and can be expressed in a power rule form as follows,

$$F_{crit} = K_0 R^{\alpha}$$

Equation 3.3

Weibull distribution has been used to model such variability [19, 23-27]. The exponent α is often related to Weibull's Modulus. The smallest particle crushing test data currently available for sand grains is around the diameter of one millimeter. Nakata et al.'s [24] data for quartz is duplicated below in Figure 3.13. Although the original data includes values for both feldspar and quartz, the decision of using just the quartz is supported by the fact that sandstones are mostly constituted by these mineral grains.

Crushing Strength vs. Particle Size
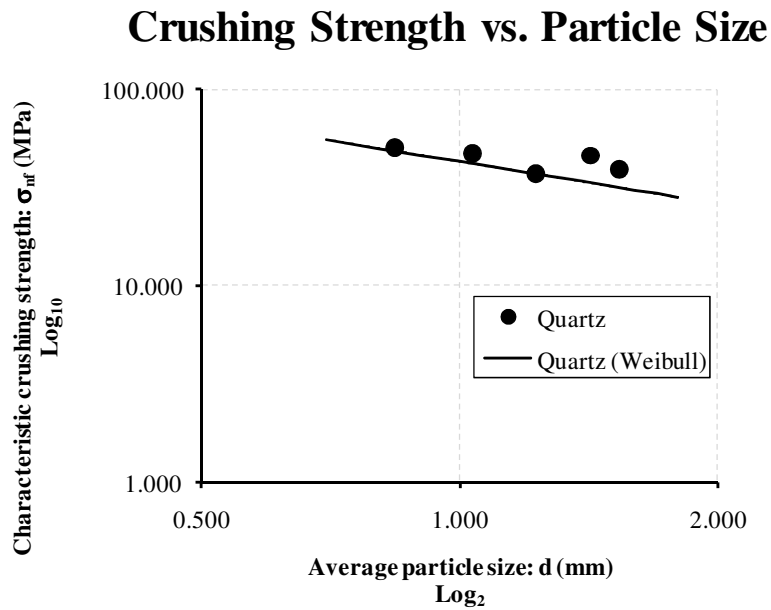
Figure 3.13 Crushing strength of quartz by Nakata et al. [24]

The Weibull distribution, Equation 3.4, is a continuous probability distribution that can be applied to failure analysis as follows: The probability of survival, $P_S(V_0)$, of a portion of similar samples to tensile stress σ with volume V_0 is given below, where σ_0 is the tensile stress

that allows the survival of 37%, i.e., e^{-1}, of the samples; and m is the Weibull Modulus, which reflects the degree of strength variability.

$$P_S(V_0) = \exp\left[-\left(\frac{\sigma}{\sigma_0}\right)^m\right]$$

Equation 3.4

A characteristic stress obtained from the Weibull distribution, where 37% of the samples having a diameter d survived, has a general form given by Equation 3.5. Using Nakata et al.'s data, an equation of characteristic crushing strength for quartz particle , σ_{nf} , was obtained as Equation 3.6, and was plotted in Figure 3.13 and Figure 3.14 as a solid line.

$$\sigma_n = \left(\frac{d}{d_0}\right)^{-3/4.2} \sigma_0 \ MPa$$

Equation 3.5

$$\sigma_{nf} = \left(\frac{d}{1.229 \ mm}\right)^{-3/4.2} 37.017 \ MPa$$

Equation 3.6

From Nakata et al.'s data, a least square power law was also obtained,

$$\sigma_{nf} = 46d^{-0.36} \ MPa$$

Equation 3.7

This equation is depicted in red in Figure 3.14. Because of the narrow range spread of the data, interpretation can vary widely.

Crushing Strength vs. Particle Size
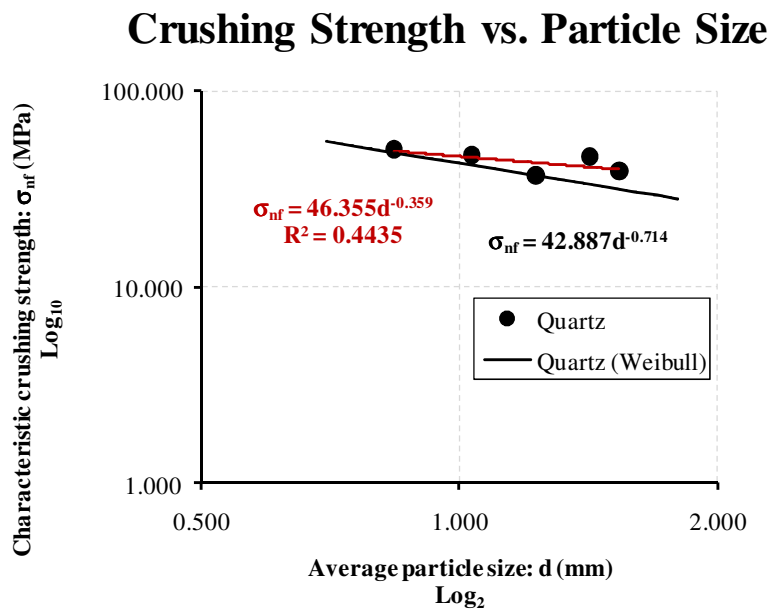
Figure 3.14 Power law and Weibull function for quartz, using Nakata et al.'s data [24]

Both set of the equations match the data , even though the equations differ drastically in that their powers are -0.395 and -0.714, respectively.

Crushing Strength vs. Particle Size
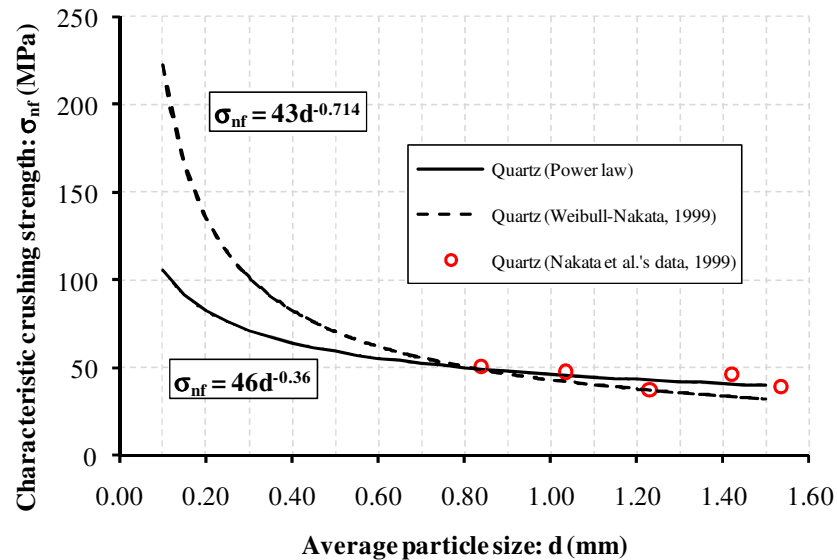
Figure 3.15 Crushing strength as a function of particle size

When extrapolate the equations to the range of particle sizes between 0.1 and 0.4 mm, focus of the study, the two equations diverge significantly as witnessed in Figure 3.15. The extrapolated strength curve is much higher in the case of the Weibull distribution. In this study, the lower power law curve was first used. One reasoning is that using quartz strength is in itself already placing strength on the high side. After all this, the strength of the particle to the crushing is driven by the power law function given in Equation 3.7 and in Figure 3.15.

As the stress and strength for crushing failure are defined, crushing of particles can be modeled. After a particle is crushed, it is replaced by many smaller particles to represent the post crushing configurations. The configuration of a crushed particle in the numerical modeling is depicted in Figure 3.16(b) where Φ, measured in counterclockwise, is the direction of the

34

maximum principal stress with respect to the horizontal; this direction represents the theoretical particle breakage.

(a)   **(b)**
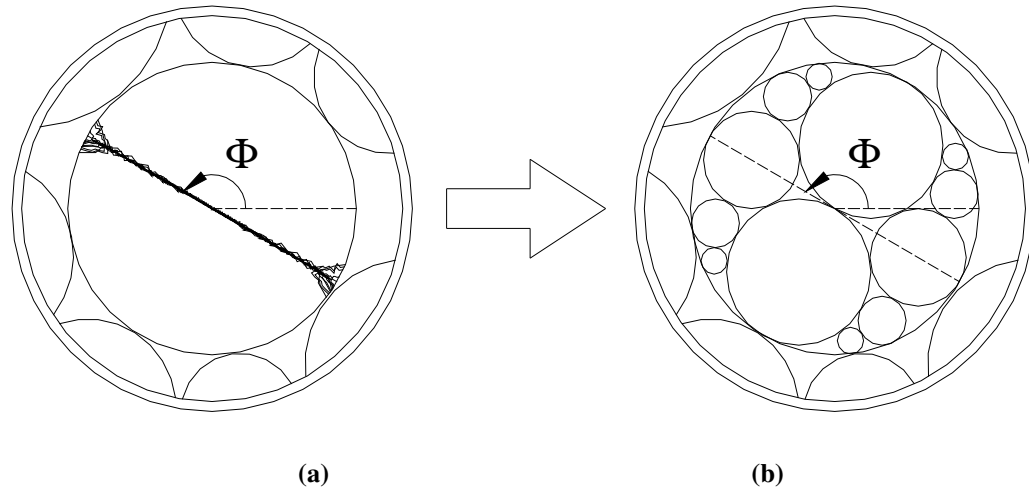
Figure 3.16 (a) Theoretical crack propagation in the particle and (b) post-breakage configuration in the DEM model (Based on Tsuongui et. al.'s work[20])

Finally, the DEM scratching simulation results shown hereafter, unless otherwise specified, include particle crushing effects.

3.3.3   Consideration of crushing mechanism in scratching test simulations

As was addressed in The Rock Scratching Test as a technique section, particle crushing is more significant around cutter tip. Therefore, in our model, the crushing failure is restricted to the particles that are near the tip of the cutter. Figure 3.17 sketches the region that particles crushing is implemented, this region is controlled by the average diameter of the particles, D_{avg}, in the *Cutting Region*.
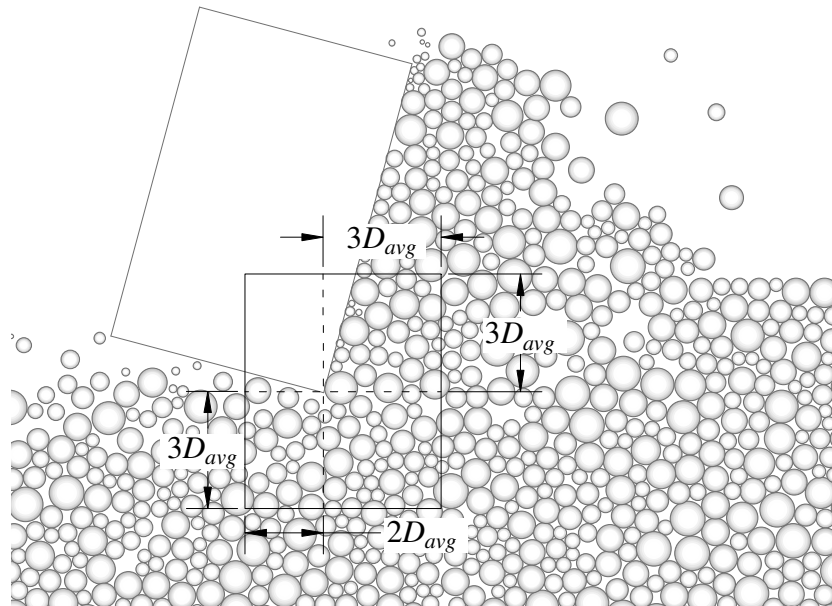
Figure 3.17 Region were crushing is allowed

This region can be visualized as a window that is fixed to the cutter and moves with it. This consideration reduces computational time significantly.

3.4   NUMERICAL SIMULATION SETUP

This section describes essential aspects of a scratch test setup, including the sample generation and the boundary condition considerations.

3.4.1 Interpretation of DEM graphical results

Various snapshots of the sample are taken during a DEM run and Figure 3.18 gives a typical such screen capture. To facilitate the discussion that follows, the meaning of the various entities in a such typical plot is explained

The plot provides a depiction of the physical characteristics: The light orange circles are the particles, the parallel black lines linking two particles represent the parallel bonds, and the inclined rectangle with black outline and white fill stands for the cutter. On top of that, the mechanical characteristics are added: The blue lines embody the contact forces, the red lines are a representation of bond breakage, and the gray and light green particles are post crushed fragmented particles.
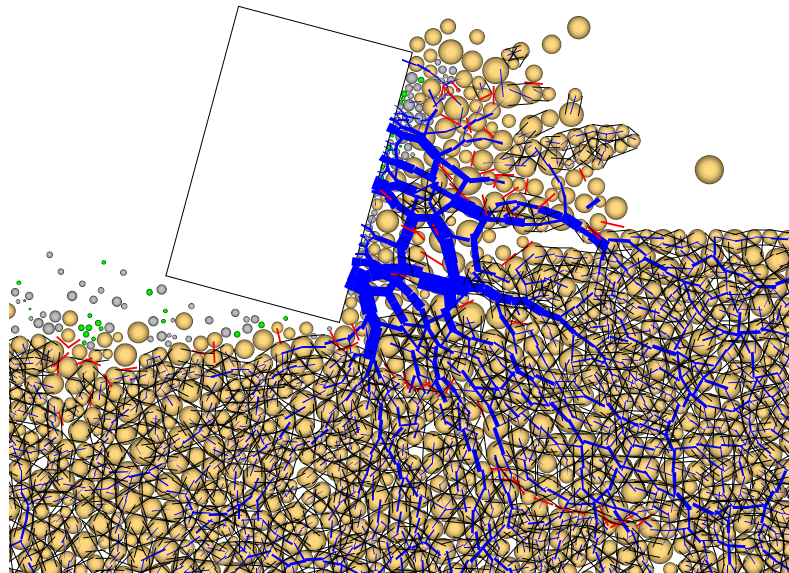
Figure 3.18 Conventions in the rock scratching DEM model

Additionally, if several red lines are coalesced into some pattern, this can generally be interpreted as a long crack being formed, like the one shown in Figure 3.18 that goes diagonally downward with respect to the tip of the cutter. Similarly, the interconnection of the contact forces in front of the cutter symbolizes the propagation of the forces in a chain form.

3.4.2   Sample preparation

As stated earlier, only in the cutter zone the actual grain size of a rock was modeled for capturing the failure mode more accurately, and beyond that, large size particles were used for reducing computational cost. Similar procedure has been suggested by Lei et al. [10, 11]. However, in creating the sample, we started by using the largest particle throughout, then gradually refined different regions so that the particles in each region were split into smaller particles

This refinement process basically converted one particle with a certain volume into two particles whose volume summation is equal to the that of the original particle. The new two particles are created in such a way that they are in contact but not overlapping, and the contact is placed in the center of the mass of the original particle. Finally, the direction of the particles is determined in a random fashion. This refinement process can happen as many times as one determines in a predefined region.

In our study, four refinement regions were predetermined: The *Cutting Region*, which is the largest region, where the refinement process was executed four times; (2) in the second region (immediately below), refinement was carried out three times; (3) within the third region, two times; and (4) in the fourth region (bottom region), only once. Figure 3.19 shows the specimen with the refinement regions identified by different colors.

38
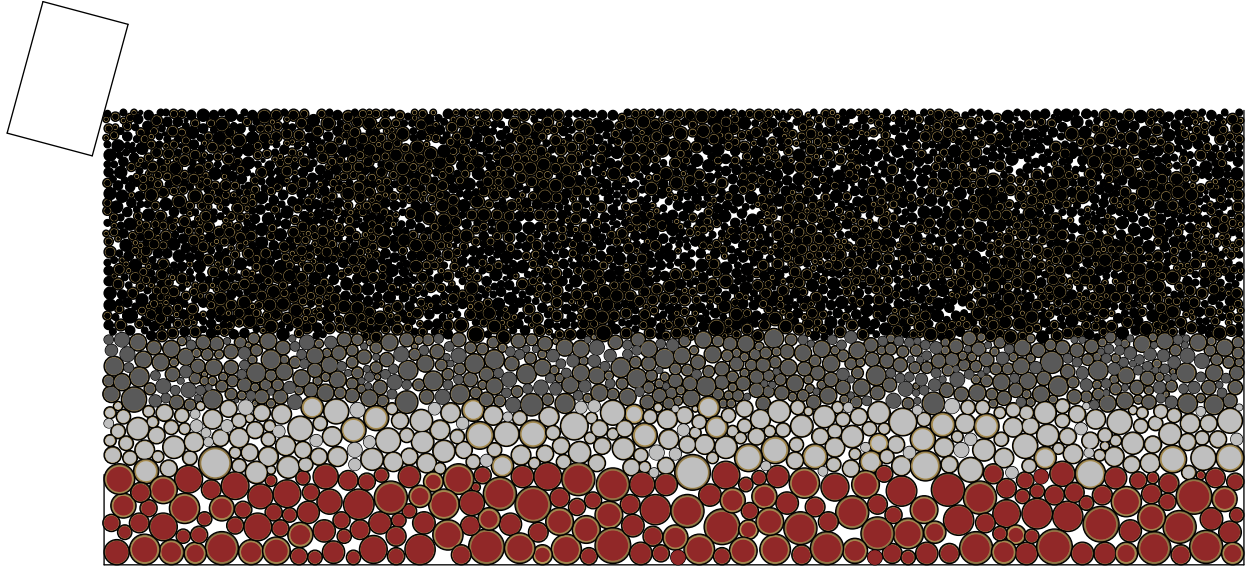
Figure 3.19 Refinement regions in the rock scratching model

Overall, the sample is created as follows:

1. *Particle Generation:* The particles are generated, with half of their designated size defined by a uniform distribution within a region delimited by walls. In order to guarantee no overlapping after rearrangement, particles that overlapped during the initial generation were deleted. Afterwards, the radii of particles are increased until they reach the target values and achieve static equilibrium under a frictionless environment.

2. *Refinement Procedure:* The particles are refined as many times as specified. Then a rearrangement is performed followed by a increasing of the particle's radius and finally a reaching of static equilibrium of the particles in frictionless environment as described in the previous step.

3. *Achieving an Isotropic Stress:* In this step the radius of each particle is increased until a specific isotropic stress is reached. In this process it is recommended that

the isotropic stresses correspond to 1% of the ultimate strength of the rock be maintained otherwise if the stress is too high the bonds may fail immediately after their creation. After the confinement, a portion of particles could be floating, i.e., particles with less than three contacts. Hence, these are then modified by fixing the velocity of the non-floating particles to zero, the radii of the floaters is largely increased, and then contracted until its contact forces with neighbors satisfy a tolerance, i.e., one-tenth of the system contact force average. When the tolerance is satisfied, the contraction stops and the floater particles gain more contacts.

4. **Installation of the Bonds:** After all the floaters are modified, the system of particles is densely packed and all the particles are in contact. At each contact, a bond is introduced, and the rock sample is created.

The various stages of the process are further illustrated in Figure 3.20.
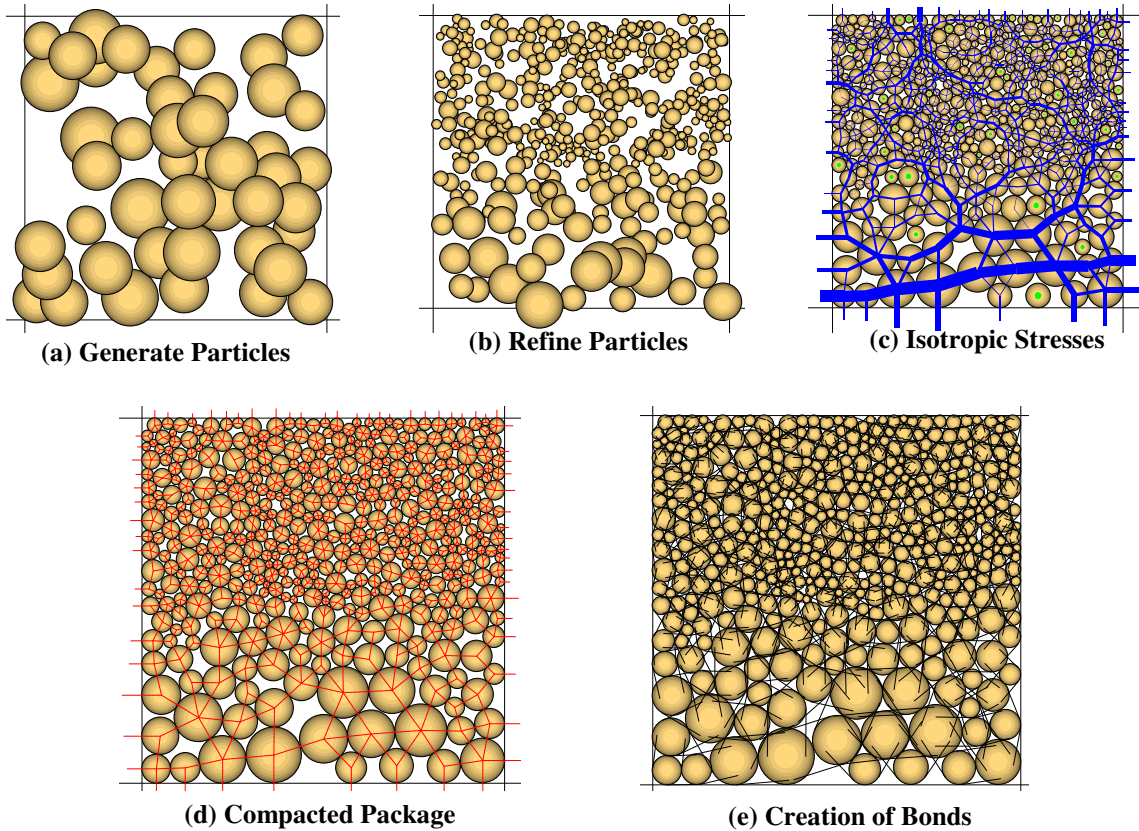
Figure 3.20 Steps for rock cutting sample preparation: (a) Generation of Particles, (b) Refinement of Particle, (c) application of Isotropic Stresses and identification of floaters, (d) Compacted Package and (e) Creation of Bonds

3.4.3   Boundary and initial conditions in the RST simulation

The boundary conditions (BCs) in a DEM system can be imposed by walls, particles and gravity. The BCs in walls are given through motion, i.e., translational and rotational velocity, while the gravitational field is defined by the acceleration due to gravity, and the particles by either force, moment or motion applied to the centroid of the particles. Even though, for particles, if the velocity is not fixed it can be changed due to the law of motion when it gets in contact with another entity, i.e., wall or ball.

The specimen created is bounded by walls on the sides and at the bottom. These walls provided fixed boundary conditions (BCs). The cutter is modeled as a segmented wall that moves at a constant speed during cutting. The walls are rigid and can be assigned with a coefficient of friction. In Figure 3.21, a picture is given of the simulation while scratching is taking place. Two wall BCs are indicated and numbered. The number (1), is indicated for walls at zero velocity, while the number (2) is assigned to a segmented wall, mimicking the cutting tool, where the translational velocity is specified, but the rotational velocity is zero.
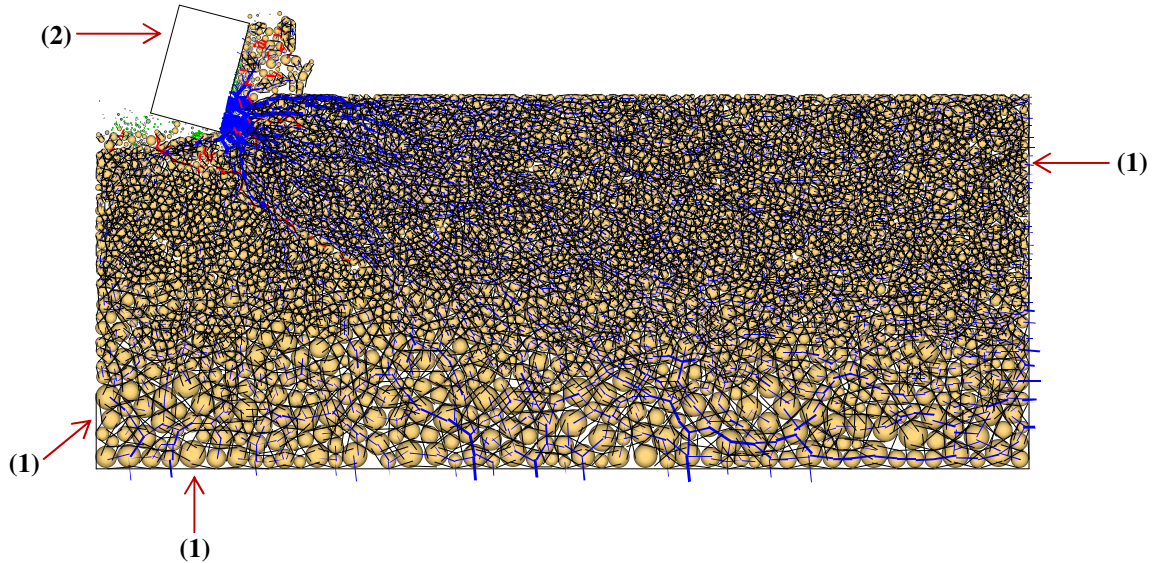
Figure 3.21 Boundary conditions in the rock scratching model

Walls have normal and shear stiffness just like balls. In this study, the stiffness of the walls was assigned a value 10% larger than its counterpart of the balls. The friction coefficient between the walls at zero velocity and the particles is set as 0.1.The impact of the coefficient of friction between the cutter and the particles is analyzed in the section Friction sensitivity.

3.5 IMPORTANT FINDINGS

Summarized herein are the most important results found throughout the research on the factors that affect the simulation results considerably. These factors include the cutter velocity and wall friction, among others. Also, the cutting forces found via the numerical model are compared to those of the physical cutting tests. Moreover, the cutting specific energy is related to the ultimate strength of the different materials created, and these results are compared with the ones obtained via the RST [3].

3.5.1 Force processing

Richard [3] found that in a shallow RST, where the failure is characterized as ductile, the pattern of the cutting forces mimics that of a white noise signal. Thus, signal processing was the approach adopted for finding a mean force. However, a different technique was taken in the present research.

The main concept adopted from Richard [3] is the fact that when the failure mechanism is ductile the cutting force can be represented by an average value. In this study, the concept of mechanical work given in Equation 3.8 was adopted to obtain that average force. The accumulated mechanical work exerted by the cutter on a rock sample up to a cutting distance x is simply

$$W(x) = \int F dx$$

Equation 3.8

Values of horizontal force were created randomly within a range through a distance as shown in Figure 3.22(a), emulating the results of the RST under ductile failure. Since the cutter moved horizontally, the mechanical work done by the cutter is simply the multiplication of the horizontal force with the horizontal movement of the cutter. The mechanical work for the given force history is obtained and presented in Figure 3.22(b).

Horizontal Force

(a)
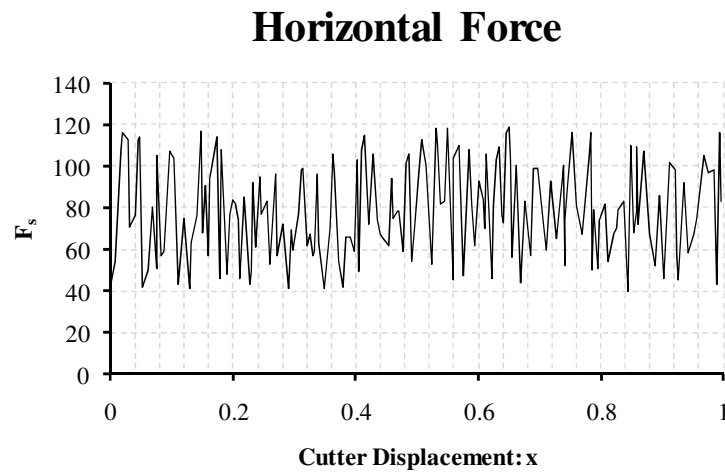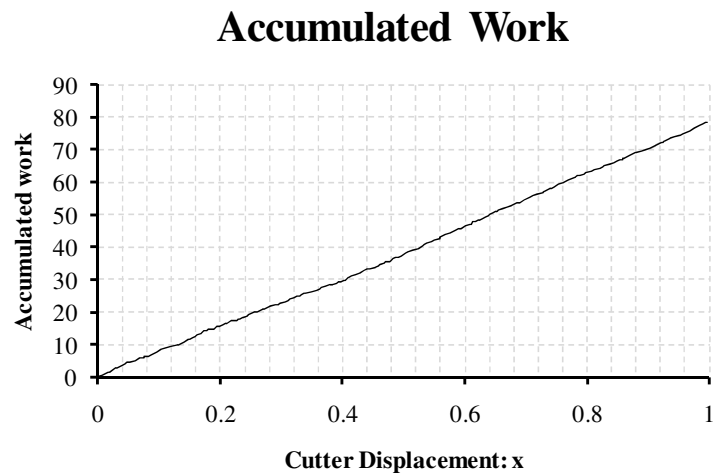
Accumulated Work

(b)

Figure 3.22 (a) Forces generated randomly in a range through a distance, and (b) accumulated word due to these forces

44

Despite the fluctuation of the force with cutting distance, the accumulated work clearly shows a linear tendency. The slope of the linear trend gives the average force of interest. A linear fit to the data can easily be made as illustrated in Figure 3.23(a). This force obtained from the slope of the linear fit is plotted in Figure 3.23(b) and it provides a good representation of the average force.

Accumulated Work

$W = 76.818x$
$R^2 = 0.9993$

(a)

Horizontal Force

76.818
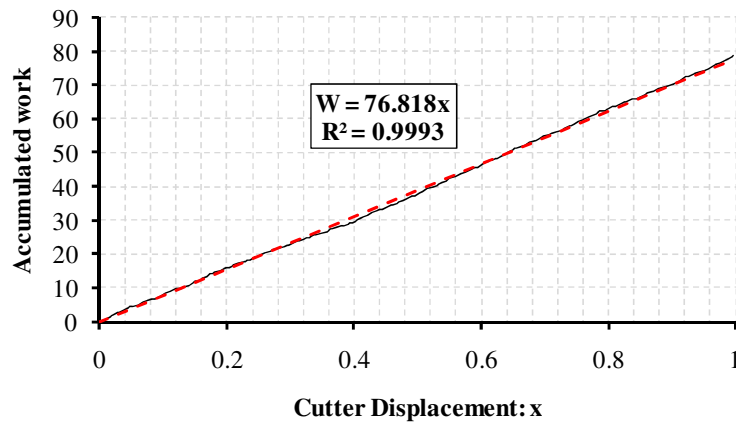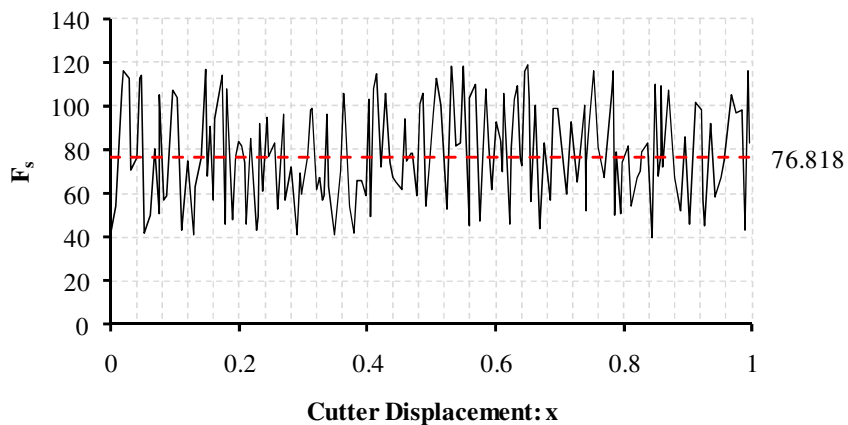
(b)

Figure 3.23 (a) Linear regression of the accumulated work, and (b) depiction of mean force obtained via mechanical work concept

3.5.2   Adjustment of critical factors

Cutter velocity and the cutter friction were found to impact greatly on the results of the cutting forces and the fragmentation process. Sensitivity studies were carried out to further pinpoint their effects. It was found, unexpectedly, that the heights of cutters used in the modeling had some influence on the results. This issue was resolved first before the sensitivity study was carried out.

3.5.2.1 Achieving a steady particle flow

Although the general focus that has been taken for simulating the RST in two-dimensions, this has an important implication with respect to the reproducibility of the cutting forces. In the actual physical laboratory test, when a rock is scratched some chipped fragments, or debris, would fall off to the side and their accumulation in front of the cutter would be more or less constant. This debris falling off phenomenon turned out to have important impact.

In the present 2D modeling, a study of the cutter force time history easily reveals that the cutter forces obtained appear to increase as the cutter advances. It was determined this was caused by the continuing debris accumulation in front of the cutter. To model the physical test correctly, we shortened the height of the cutter to reflect the height of potential debris accumulation deleting the particles above the cutter. A comparison between Figure 3.24(a) and Figure 3.24(b) affirms that the use of a short cutter resolves the debris accumulation problem, and the force pattern ceased to show an ever increasing trend. This revision actually put the cutter model closer to the cutter size used in the laboratory as presented in Figure 3.1(a).
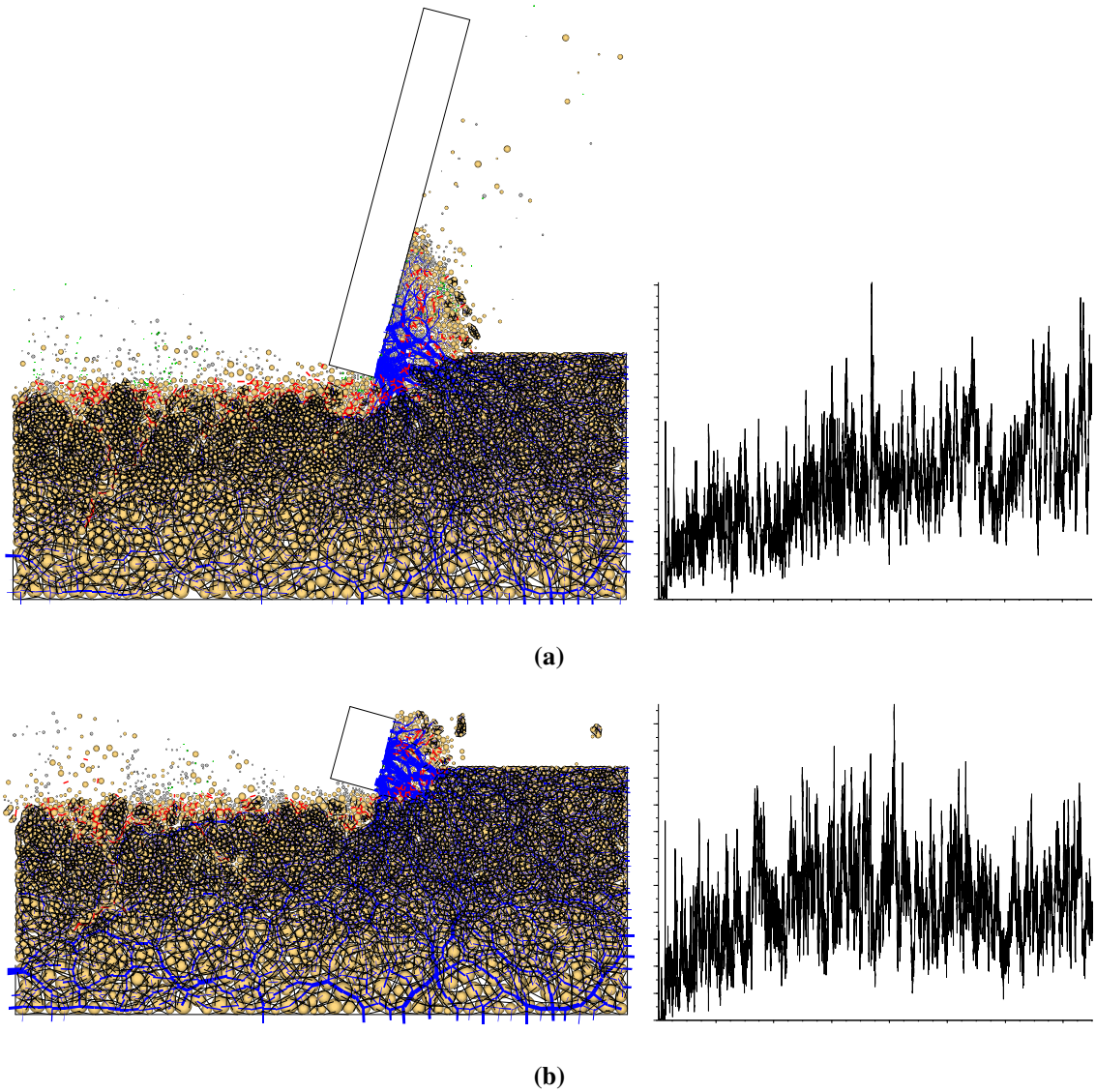
Figure 3.24 (a) Effects of debris accumulation on both the configuration and cutting forces; and (b) effect of short cutter and particle deletion on both the configuration and cutting forces

3.5.2.2 Impact of cutter velocity

There has been no research done previously on how to find an appropriate cutting velocity in the modeling. For instance, Lei et al. [10, 11] used a cutting velocity of 1 *m/sec* in rock cutting while Tan et al. [28] used different velocities (5, 10 and 15 *m/sec*) and analyzed only the impact of cutting velocity on the crack formation behavior of cutting into polycrystalline SiC.

In an effort to model the RST conducted by Richards in which the laboratory tests was conducted with a cutting velocity 4 *mm/sec* [3], the following was considered. From DEM perspective, this velocity is untenable for the computational time step is often in the order of 5×10^{-9} seconds because of the high stiffness of the contact springs. The 4 *mm/sec* velocity would require 5×10^{7} steps of computation just to advance the cutter by 1 mm. Also, a precise cutting velocity also requires a precise matching of damping in the system which is simply not available.

A practical approach taken up in this study is to adopt the default damping and search for the right cutting velocity that may reproduce the results of the laboratory tests. The default value for the local adaptive damping coefficient in the PFC2D was 0.7. Then, conduct simulation with cutter velocities ranging from 0.25 to 3.00 *m/sec* and both the failure behavior and the cutting forces' magnitude were observed.

Figure 3.25 shows a comparison in the failure configuration, accumulated work and the cutter force results obtained, respectively, for the slowest and the fastest cutting velocities modeled.
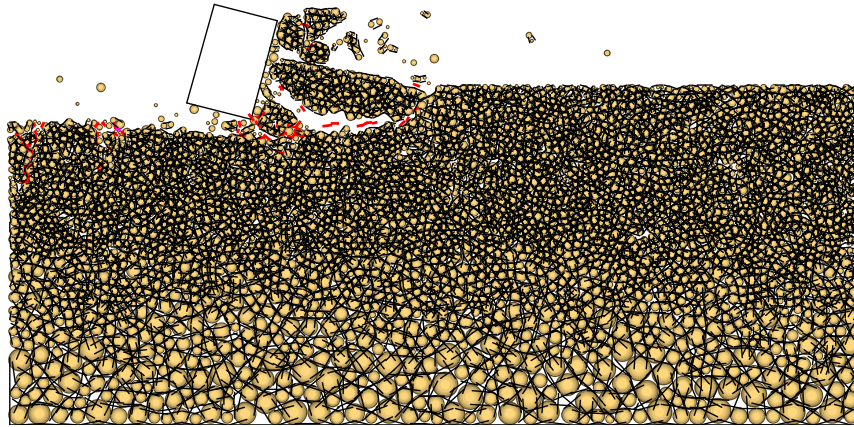
$v_c = 0.25$ m/sec

Accumulated Work

$W_A = 3.5805x$
$R^2 = 0.9796$

W_A (kN-m)

Cutter Displacement: x (m)

Horizontal force

F_s (kN/m)

3.5805

Cutter Displacement (m)

(a)

49

v_c = 3.00 m/sec

Accumulated Work

$W_A = 49.335x$
$R^2 = 0.9964$

W_A (kN/m)

Cutter Displacement: x (m)

Horizontal force

49.335

F_s (kN/m)

Cutter Displacement (m)
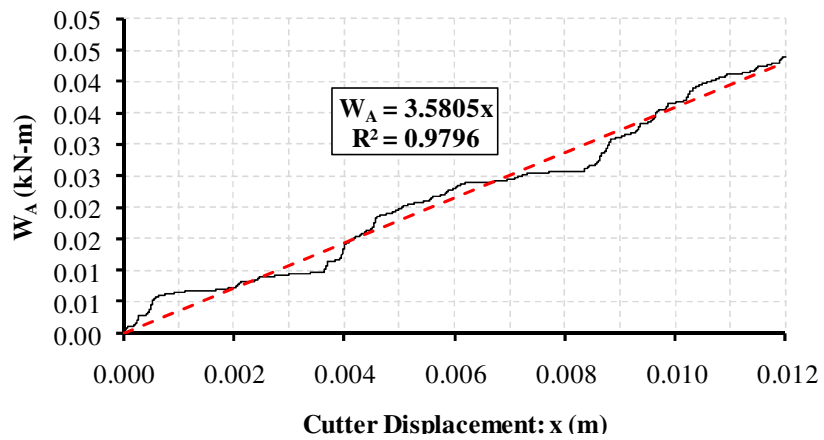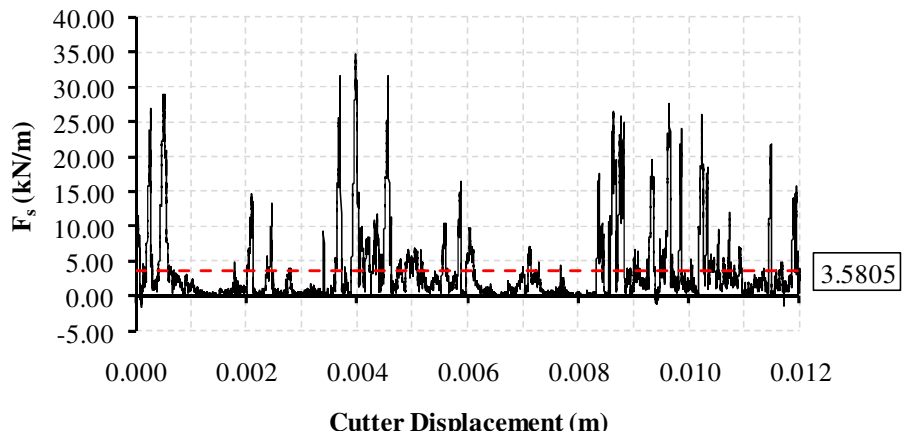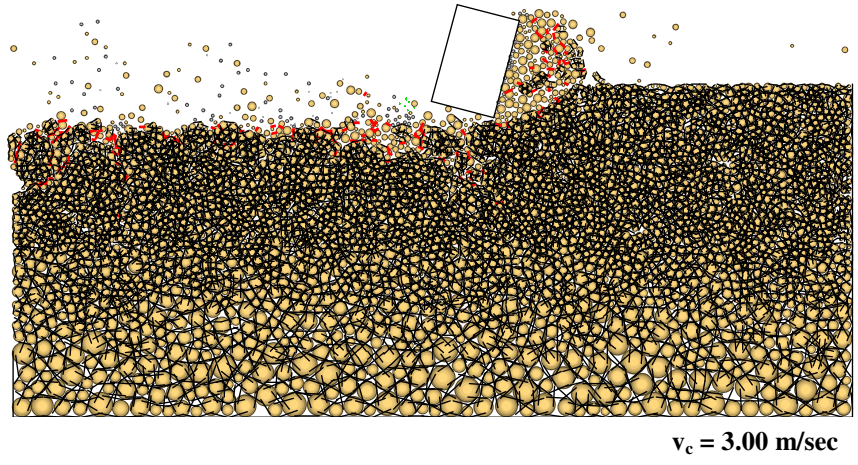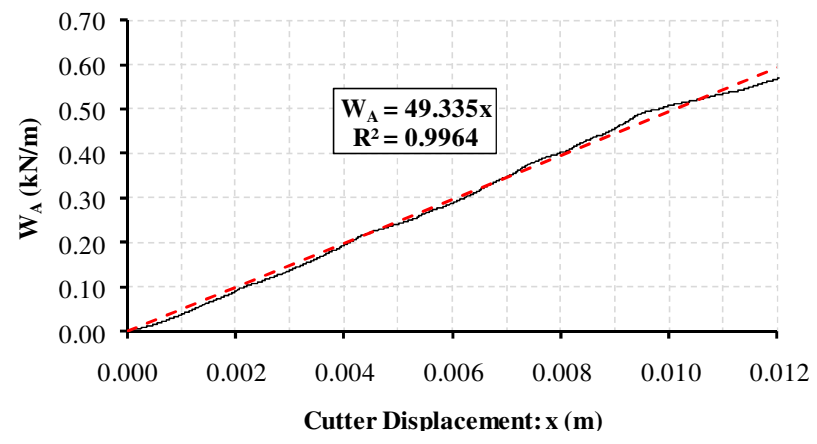
(b)

Figure 3.25 Velocity influence in the rock scratching test at (a) 0.25 m/sec and (b) 3.00 m/sec

The difference in the failure mode is striking, and it is thought that the reason for a chip developing under slow velocity is because the forces can propagate, seek, and destroy the weakest bonds, while in the high speed failure force propagation is lesser, leaving no choice than failed immediate bonds. Moreover, the propagation of cracks towards the bottom is a signal that has been reported as characteristic in shallow failure. A further study on the forces indicates that the white noise pattern is not developed under small velocities; this is understandable due to the loss of contact when the failure is more like a brittle, than like a ductile flow. This is also reflected in the accumulated work, where some horizontal tendencies are noticed, meaning there are no forces while the cutter advances, *ergo*, no work is performed. Therefore, the concept of mechanical work cannot be adopted for processing the forces, and clear proof for this is the somehow meaningless mean force obtained from the linear regression of the accumulated work. On the other hand, the force pattern and the accumulated work of the high velocity case looks much more results that can be compared with the physical tests.

It is clear that higher velocities might lead us to the correct answer, but the mean force for the 3 m/sec case seems too high taking into account the ultimate strength of the material, i.e., *SS_25_I*. Figure 3.26 shows the results of the simulations performed expressed in terms of accumulated work and mean force. The force that we might find comparable sho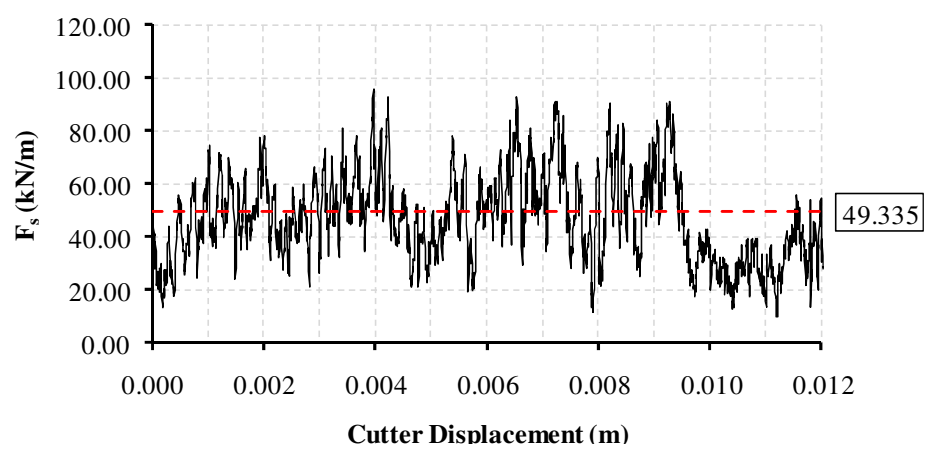uld be close to the results obtained by Richard [3], which suggests that the cutting force for a rock with an UCS around 30 *MPa* should be in the order of 30 to 36 *MPa* as given in Table 3.6. Hence, the velocity chosen for our simulation is 2 m/sec, and the results of the configuration and the cutting forces are shown in Figure 3.27. This velocity of 2 m/sec was afterwards applied to all the modeling work.

51

Accumulated Work

(a)
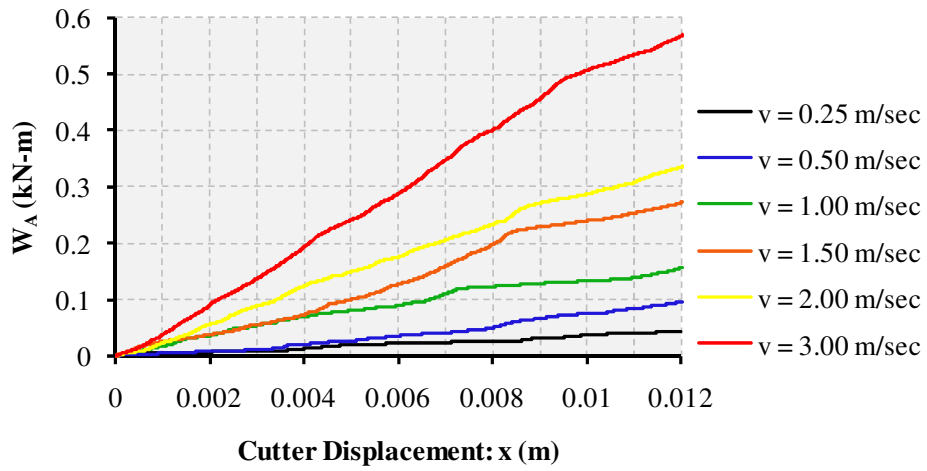
Horizontal force (Mean Force)

$$F_S = 15.671v_c$$
$$R^2 = 0.9902$$
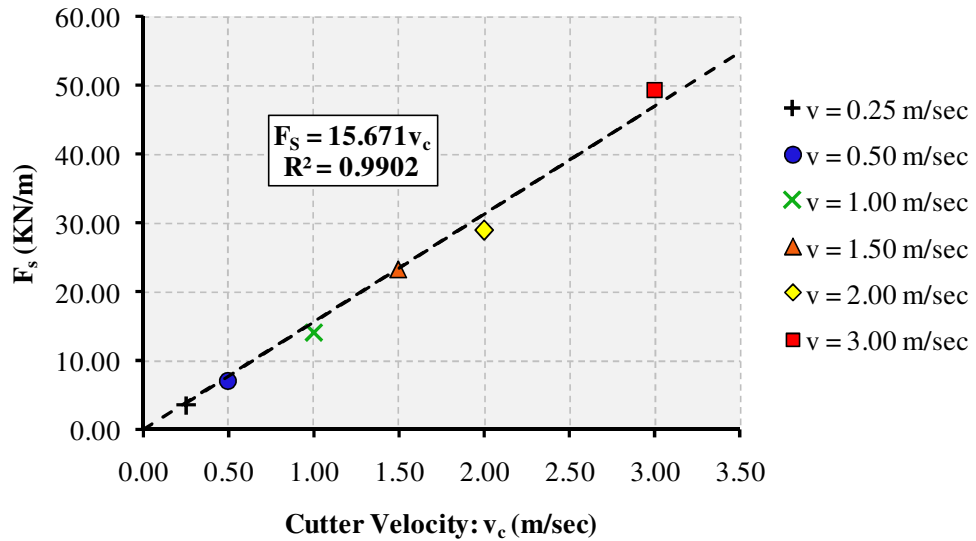
(b)

Figure 3.26 Results at different velocities of (a) accumulated work and (b) mean horizontal force

Table 3.6 Results obtained from Rock Scratching and UCS Tests by Richard [3][2]

Rock	σ_c (MPa)	F_s (kN/m)
A2-4	9	13
Elgin 5563.33 m	12	16
Redwildmoor sandstone	13	17
Castelgate sandstone	15	22
Chalk	17	16
A2-6	18	20
A2-3	20	18
Elgin 5587.9	21	20
Lf6	24	23
Lf7	28	27
Chauvigny limestone	29	36
Elgin 5575.66	33	29
Elgin 5660.9	37	43
Vosges Sandstone	42	32
A3-10	43	38
A2-7	46	35
Elgin 5523.22	46	20
Elgin 5684.2	47	40
Elgin 5608.8	50	30
Elgin 5623.6	51	51
Elgin 5672.7	68	58
Buxy limestone	78	66
Fontainebleau sandstone	110	85
Rhune sandstone	110	122

---

[2] The original results are shown in terms of specific energy instead of horizontal forces, but were converted

for comparison purposes taking into account that the cutting depth of our model is 1mm and unit depth is 1 m.

SS_25_I

(a)

Horizontal force

29.028
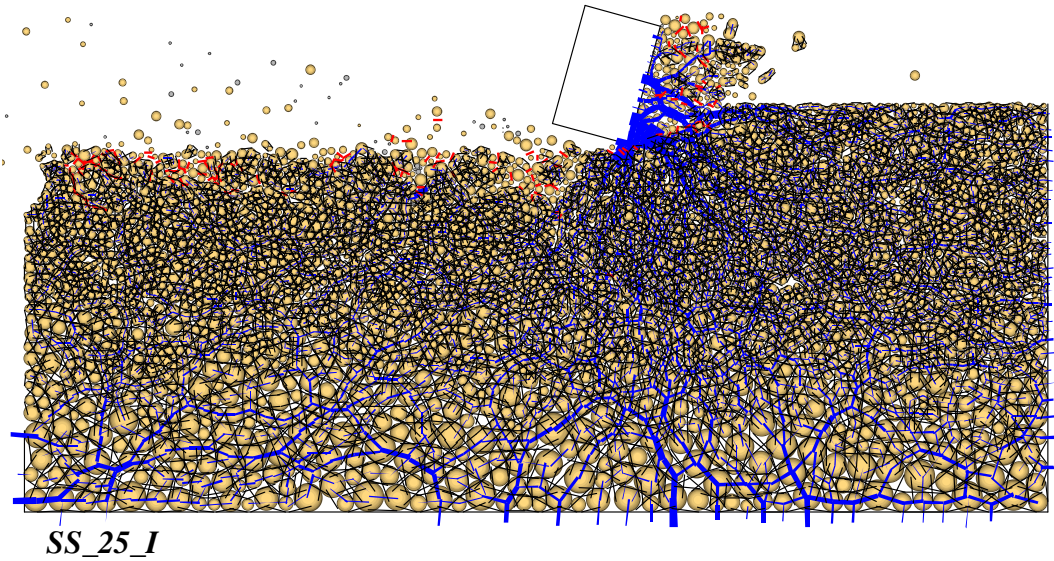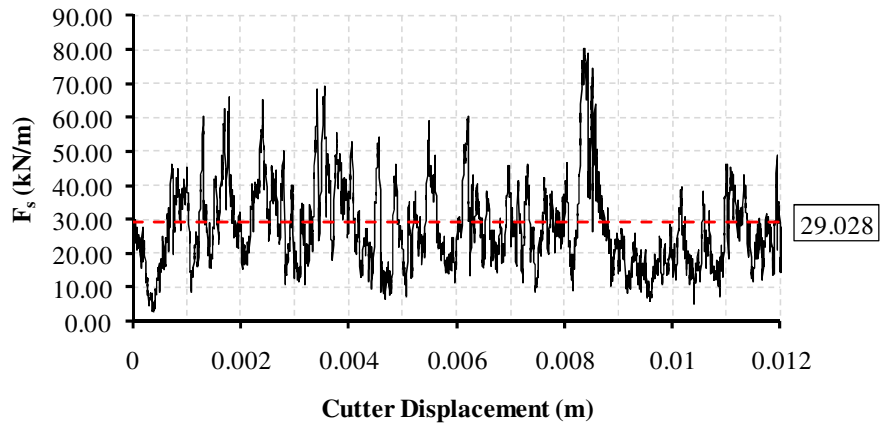
(b)

Figure 3.27 (a) A snapshot of the RST simulation at 2.00 m/sec and (b) its respective horizontal forces

3.5.2.3 Impact of cutter friction

In a rock scratching test, the influence of cutter friction was studied by Dagrain & Richard [29]. From this study, it was observed that the coefficient of friction between polished PDC bits and different types of rock ranges around 0.18 and 0.37. Moreover, a further study was carried out on

54

the influence of the friction coefficient, μ, between the cutter and the rock specimen. Three different μ were used, namely, 0.00, 0.25 and 0.50 The effects were investigated in terms of failure configuration and the resulting cutter forces are summarized in Figure 3.28.

SS_25_I

Horizontal force

29.028

(a)

SS_25_I

Horizontal force

31.146

Cutter Displacement (m)

(b)

SS_25_I

Horizontal force

49.335

Cutter Displacement (m)
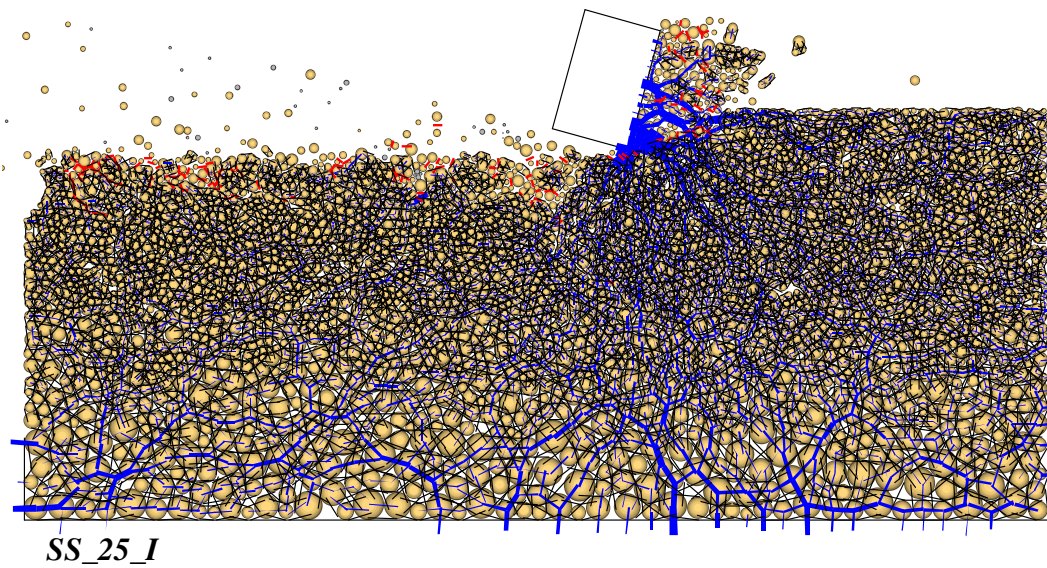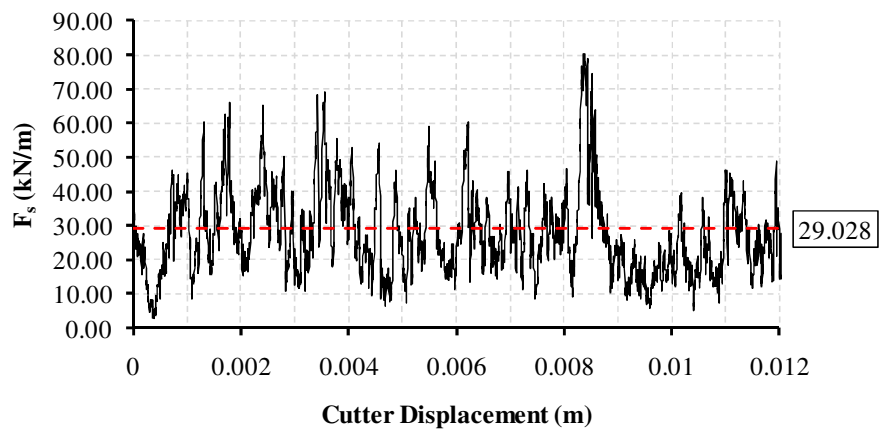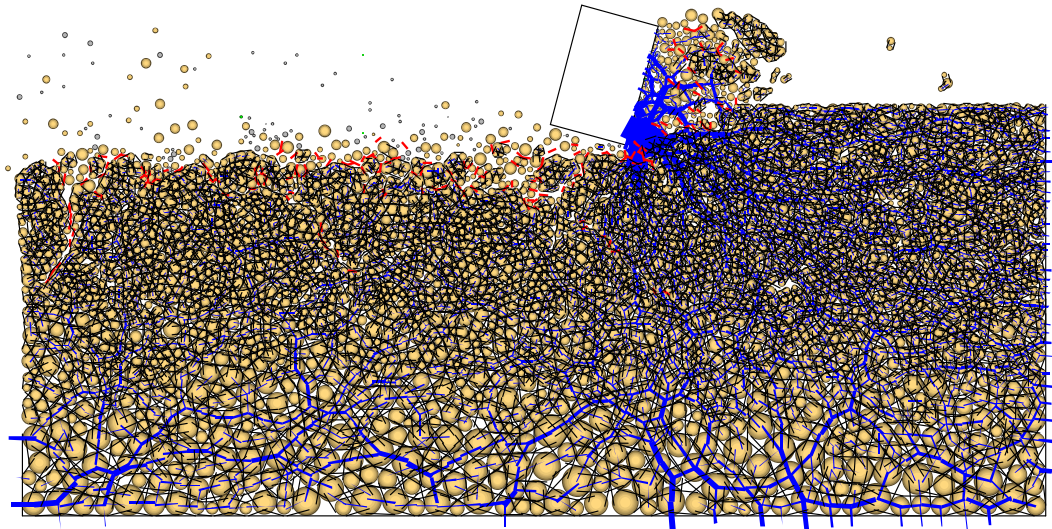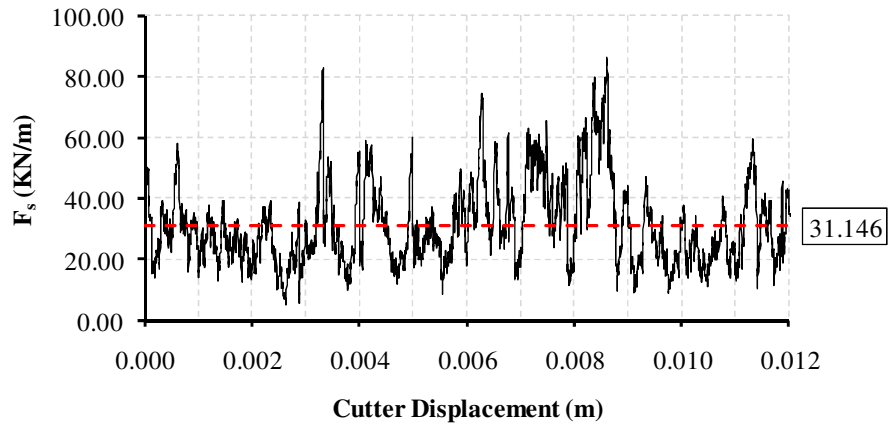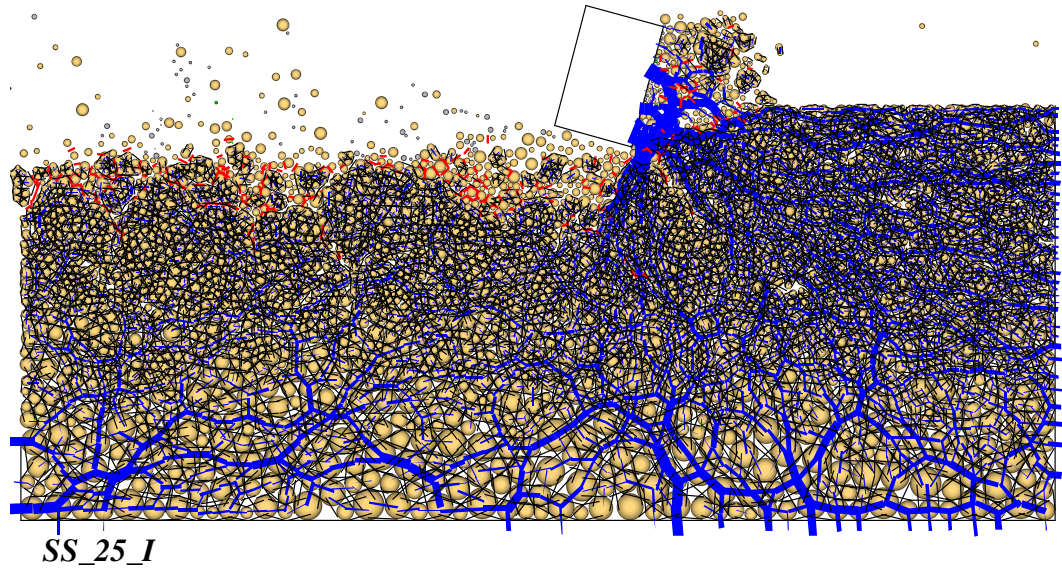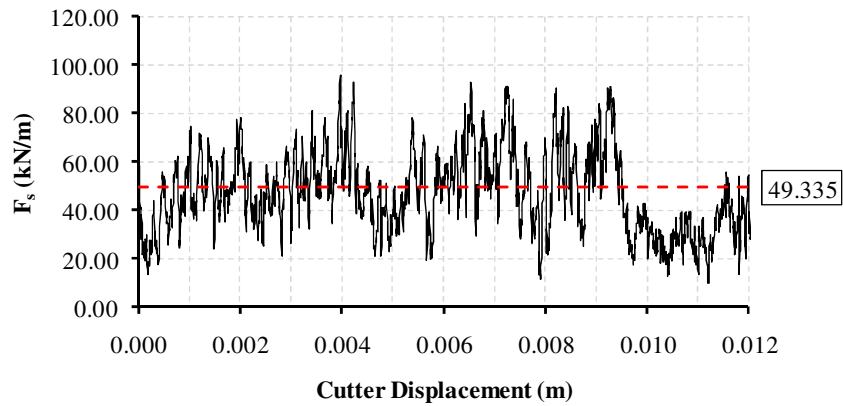
(c)

Figure 3.28 Configuration and cutting forces under a coefficient of friction between the cutter and the

specimen of: (a) 0.00 (b) 0.25 and (c) 0.50

It is concluded that the use of a μ of 0.25 offers a best choice with respect to the other

cases: (1) the cutting force increases only slightly over zero frictional case and remains the same

level as those given in Table 3.6 for the rock strength, whereas the 0.5 friction pushes the cutter

force too high, and (2) the failure mode has the feature of developing macro-cracks towards the

bulk, which is not observed for the zero coefficient of friction. Therefore, the μ of 0.25 was employed for the analysis

3.5.3   A discussion on cutting forces obtained

The force pattern obtained in our model has been consistent with that obtained by Richard [3] as exemplified by Figure 3.29. However, the aim is to find if the cutting force magnitude of our simulation is comparable with the ones obtained in the physical laboratory test. In addition, the results shown in Figure 3.29 summarizes the cutting force time history of a Vosges sandstone subjected to a 0.3 *mm* depth of cutting, and the rock has an UCS of 42 *MPa* (Refer to Table 3.6).
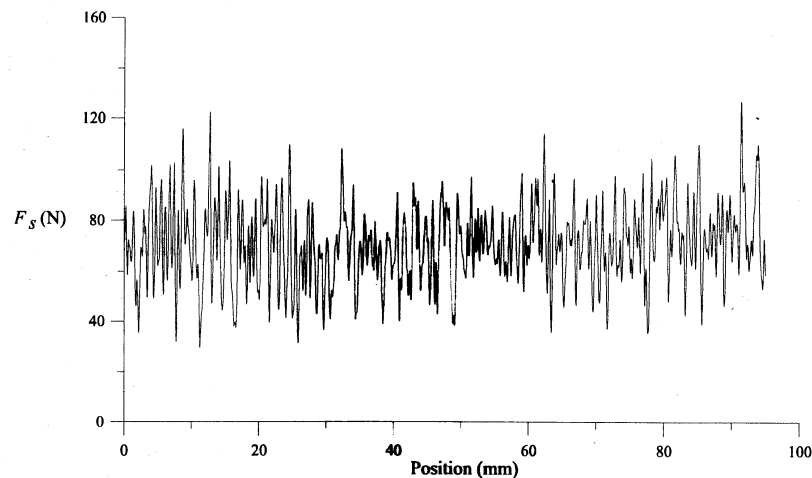
Figure 3.29 Horizontal forces of a RST performed in a Vosges sandstone at 3 *mm* of depth cutting by

Richard [3]

For the Vosges sandstone, Richards [3] has also shown that the magnitudes of the cutting force are proportional to the depth of cutting. His results are summarized in Table 3.7.

58

Table 3.7 Results obtained from RST on a Vosges sandstone by Richard [3][3]

d (mm)	d (m)	F_S (N/10mm)	F_S (kN/m)
0.2	2.00E-04	30	3.0
0.3	3.00E-04	63	6.3
0.4	4.00E-04	104	10.4
0.5	5.00E-04	126	12.6
0.6	6.00E-04	147	14.7
0.7	7.00E-04	170	17.0
0.8	8.00E-04	193	19.3
0.9	9.00E-04	225	22.5

The author found that the cutting force is proportional to the cutting depth when the failure mode has ductile characteristics. Thus, a linear regression of the data given in Table 3.7, shown in Figure 3.30, projects the average cutting force to be around 24.4 *kN/m* for a 1 *mm* cutting depth. Based upon this data, and with the observation that 1 *mm* cutting depth in our simulation still exhibits the ductile mode of failure, we compare the forces from our 1 *mm* cutting depth analysis results with this projected value.

---

[3] An extra column for cutting force in our units is added.

Horizontal Force vs. Cutting depth
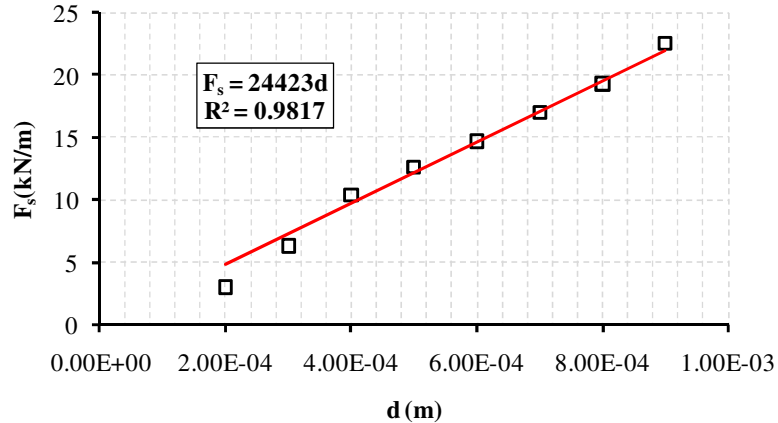
Figure 3.30 Cutting forces at different depths in a Vosges sandstone (Data taken from Richard [3])

Our specimens derived from *SS_25_I* and *SS_25_II* are compatible to the Vosges sandstone, even though the UCSs of these materials are slightly smaller at 29.95 and 35.31 *MPa*, respectively. But this is not deemed a substantial difference as the strength of a given rock has a high variability because of their inherent heterogeneous nature.

A case in point, Bésuelle [30] has obtained a $\sigma_c \approx 35\,MPa$ for the same sandstone. In Figure 3.31 the results of the horizontal cutting force time history and the mean cutting forces of *SS_25_I* and *SS_25_II* specimens are depicted. From here, our cutting forces obtained were of the same order of magnitude that the one obtained previously from Richard's data ($F_S \approx 24.4$ *kN/m*). In conclusion, the response obtained in the simulation of the RST, from materials that have similar mechanical characteristics to the ones from Vosges sandstone, shows a strong similarity in both force magnitude and force pattern, with respect to the physical laboratory test results.

Horizontal force

(a)
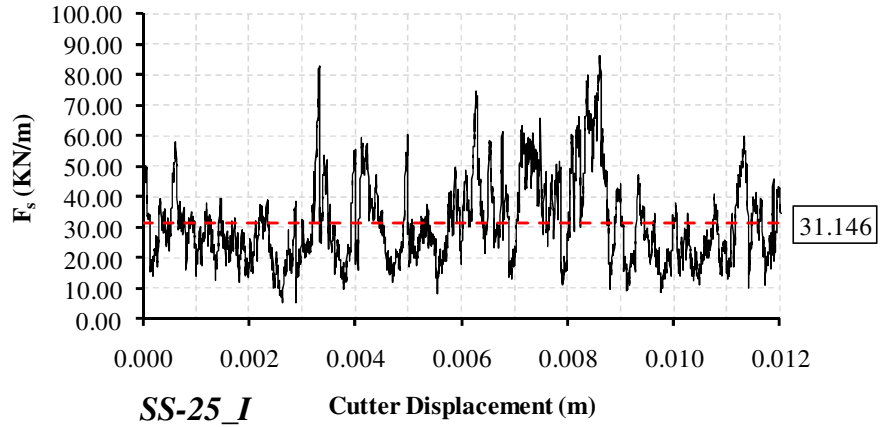
Horizontal force
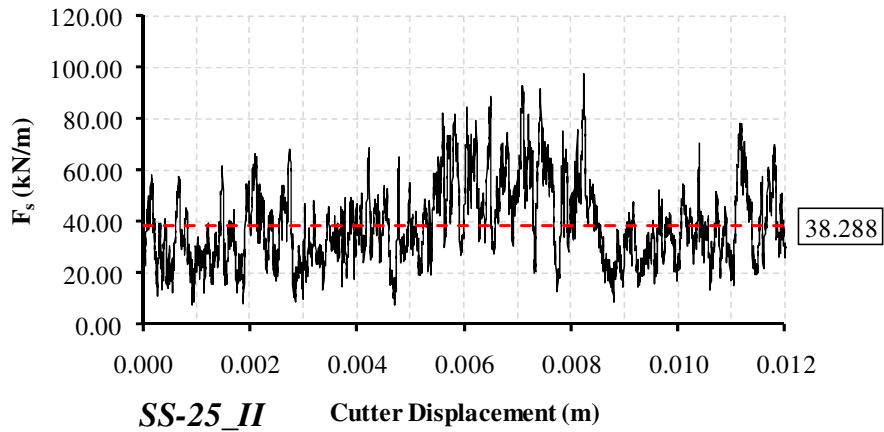
(b)

Figure 3.31 Cutting force history obtained from the materials (a) *SS_25_I* and (b) *SS_25_II*

An illustration of the ability to model the fragmentation process, is presented with a side by side comparison of the laboratory test and modeling results. Shown in Figure 3.32(a) is a snapshot of a shallow cut laboratory scratching test on a Berea Sandstone [3], while Figure 3.32(b) is taken from our DEM simulation. Thus, our model appear to be able to capture the characteristics of the fragmentation process.

(a) **(b)**
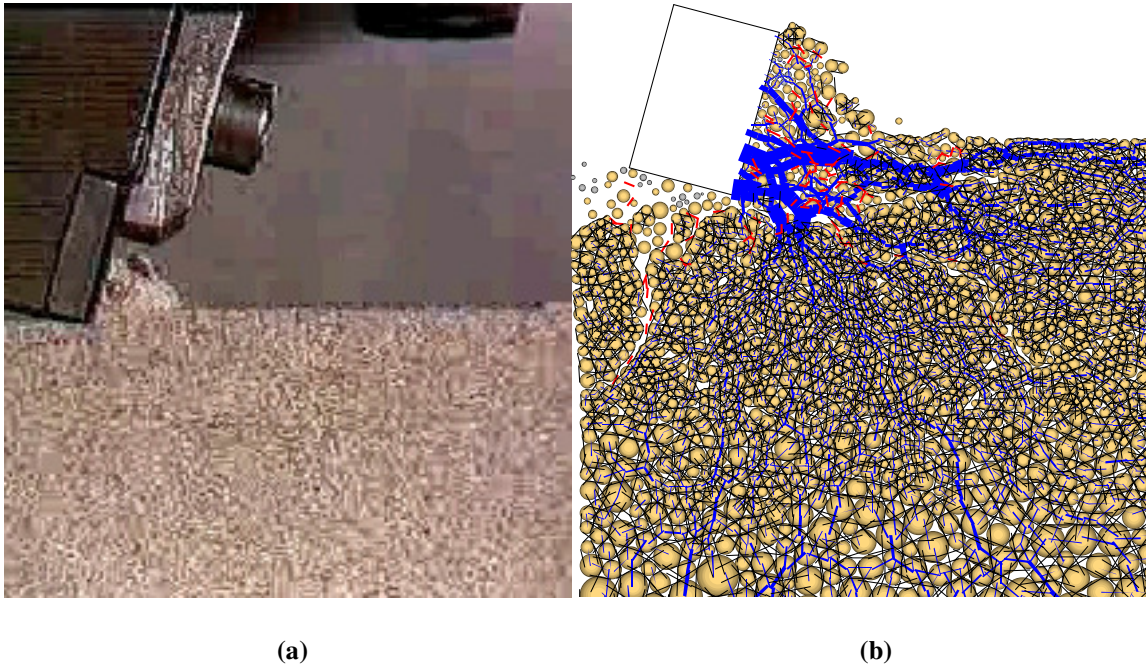
Figure 3.32 Failure mode comparison: (a) laboratory test [3] and (b) DEM simulaiton

3.5.4   Results obtained on a suite of tests

One of the important findings from Richard [3] on shallow scratch tests is that the specific energy input required from the cutter to advance is proportional to the uniaxial strength of the rock. Based upon this result, it also suggest scratch test be used as an alternative way of measure the UCS of rocks. A more credible validation of the present study would be to reproduce that result through DEM. For this purpose, scratch tests were carried out on a suite of tests on eight different simulated rock materials, and the results obtained are summarized in Table 3.8 for the mean cutting forces, F_S.

Table 3.8 RST cutting forces obtained for the different materials

Material	$F_{s_{\mu=0.25}}$ (kN/m)
SS_25_I	31.15
SS_25_II	38.29
SS_50_I	56.40
SS_50_II	63.71
SS_75_I	84.29
SS_75_II	69.09
SS_100_I	70.08
SS_100_II	69.09

The specific energy, ε, is defined as the energy required to cut a unit volume of rock. For the 2D analysis carried out here, it can be computed as the force over the projection of the contact area. Results obtained by Richard [3] of several RSTs performed in different rock types are given in Table 3.9. The author argues that a linear correlation between cutting specific energy and UCS is an important finding achieved through the RST. However, the dispersion of the results given by some rocks is not clearly understood, and influences from the variability of the UCS test to factors not related directly with strength measurements are suggested. In addition, it was found that the specific energy is dependent upon the geometry of the cutting tool.

The data in Table 3.9 is plotted, as can be established in Figure 3.33. Then, a simple linear regression is performed setting the intercept at zero. Richard's data can be described by the equation below.

$$\varepsilon = 0.8896\,\sigma_c$$

Equation 3.9

Table 3.9 Cutting specific energy of different types of rock obtained by Richard [3]

Rock	σ_c (MPa)	ε (MPa)
A2-4	9	13
Elgin 5563.33 m	12	16
Redwildmoor sandstone	13	17
Castelgate sandstone	15	22
Chalk	17	16
A2-6	18	20
A2-3	20	18
Elgin 5587.9	21	20
Lf6	24	23
Lf7	28	27
Chauvigny limestone	29	36
Elgin 5575.66	33	29
Elgin 5660.9	37	43
Vosges Sandstone	42	32
A3-10	43	38
A2-7	46	35
Elgin 5523.22	46	20
Elgin 5684.2	47	40
Elgin 5608.8	50	30
Elgin 5623.6	51	51
Elgin 5672.7	68	58
Buxy limestone	78	66
Fontainebleau sandstone	110	85
Rhune sandstone	110	122

Cutting specific energy vs. Rock strength

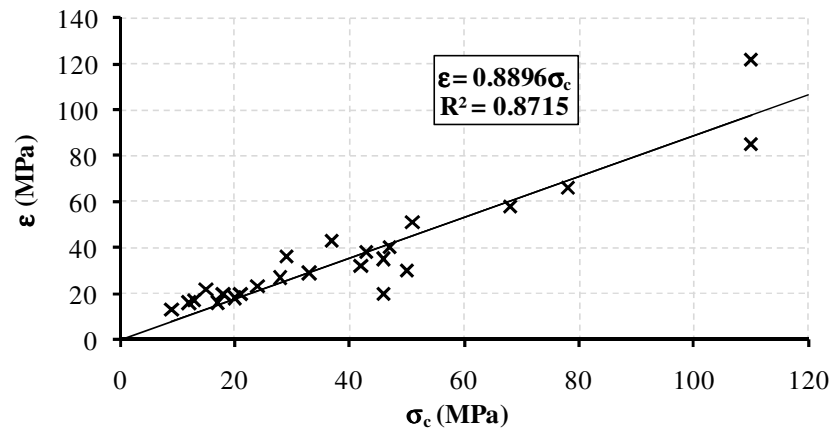
$$\varepsilon = 0.8896\sigma_c$$
$$R^2 = 0.8715$$

Figure 3.33 Cutting specific energy and rock strength linear regression (Data taken from Richard [3])

A summary of our results are given in Table 3.10. Using all the data we computed, a linear trend is obtained with a much lower slope. Upon a further investigation, it is clear that our trend is skewed by two data points as marked in Figure 3.34. The specific energy of these two data points were excessively low. An inspection of the failure configuration of the sample revealed that these two data points because of the high compressive strength of the rock, consequently high bonding strength, the rock particles were crushed before the bond got the chance to be broken. As a result, the cutting forces, and specific energy for that matter, were limited. Had these two points being removed, this study would yield,

$$\varepsilon = 0.8329 \, \sigma_c$$

Equation 3.10

as depicted in Figure 3.35. Thus, without including the particle crushing effects, this study would reproduce the general results from laboratory tests. This provides a strong validation on the present DEM modeling.

Table 3.10 Summarized results from laboratory tests and RSTs simulations

Material	σ_c (MPa)	E (GPa)	Ratio E/σ_c	$F_{s\,\mu=0.25}$ (kN/m)	$\varepsilon_{\mu=0.25}$ (MPa)
SS_25_I	29.95	4.87	162.48	31.15	31.15
SS_25_II	35.31	9.46	268.03	38.29	38.29
SS_50_I	67.65	9.27	137.09	56.40	56.40
SS_50_II	79.96	18.25	228.20	63.71	63.71
SS_75_I	88.41	13.76	155.62	84.29	84.29
SS_75_II	97.85	27.32	279.18	69.09	69.09
SS_100_I	121.42	18.17	149.66	70.08	70.08
SS_100_II	129.78	35.91	276.73	69.09	69.09

Cutting specific energy vs. Rock strength (UCS)
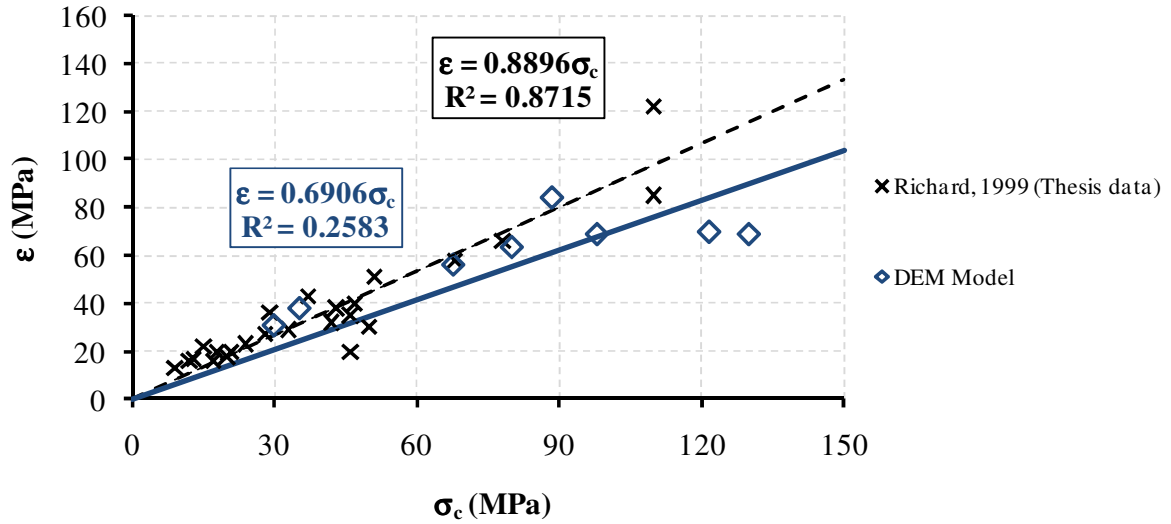
Figure 3.34 Cutting specific energy and rock strength linear regression of both simulation and physical

tests (Data taken from Richard [3])

Cutting specific energy vs. Rock strength (UCS)
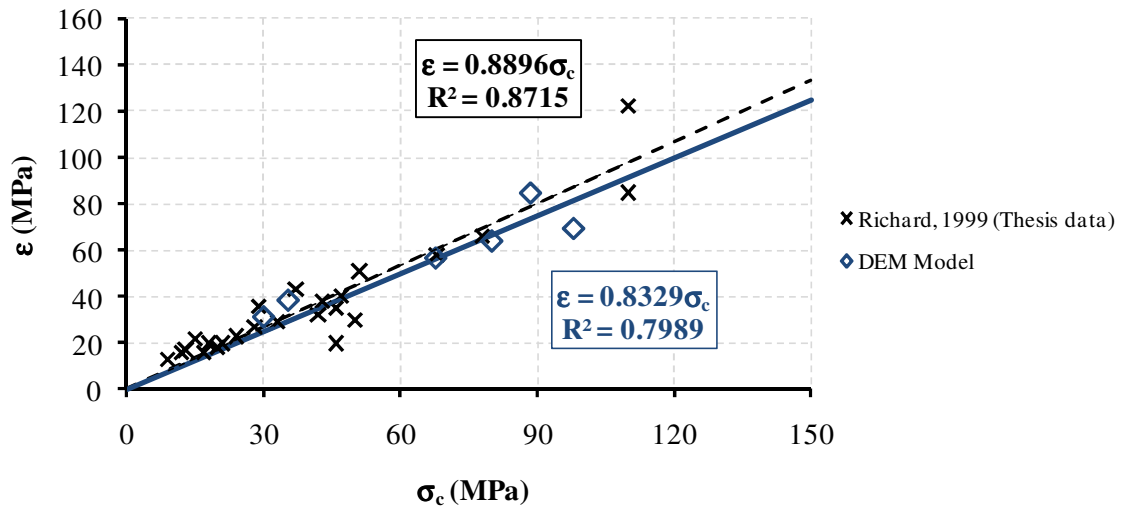
Figure 3.35 Cutting specific energy and rock strength linear regression of both simulation and physical

tests, but disregarding the data influenced by crushing strength (Data taken from Richard [3])

3.5.5   Influence on crushing

When more high strength rock samples were added to the data, we found that there is an upper bound curve of how high the specific energy can go. This is illustrated in Figure 3.36.

Cutting specific energy vs. Rock strength (UCS)

$$\varepsilon = 0.8329\sigma_c$$
$$R^2 = 0.7989$$

- ✕ Richard, 1999 (Thesis data)
- ◇ DEM Model
- – – – Crushing strength influence

Figure 3.36 Particle crushing strength influence at high material uniaxial strength

From the nature of the problem, it makes sense that there is an upper bound to the specific energy. So, if alternatively, the higher crushing strength curve in Figure 3.15 was employed, one would expect the upper bound of specific energy would be raised. This, indeed, is the case as illustrated in Figure 3.37.

67

Cutting specific energy vs. Rock strength (UCS)

Figure 3.37 Different particle crushing strength influence at high material uniaxial strength

We added two specimen which properties are given in Table 3.11, and performed scratching tests with higher particle crushing strength as extrapolated from the Weibull distribution. Using this higher crushing strength, the specific energy versus rock uniaxial strength relation is seen to be linear up to σ_c equals 130 *MPa*. When σ_c reaches around 130 MPa, the specific energy hits a plateau.

In summary, we predict the linear relationship to cease once the uniaxial strength becomes high and that particle crushing plays a significant role. The exact nature still is uncertain because of the lack of data.

Table 3.11 Summary results of Uniaxial tests from two new materials in CASES I and II

Summary	σ_c (MPa)	ν	E (GPa)	E/σ_c
Sample with 125 MPa of normal parallel bond (SS-125_I):	*177.30*	*0.17*	*22.40*	*126.34*
Sample with 125 MPa of normal parallel bond (SS-125_II):	*188.75*	*0.16*	*44.69*	*236.74*

In addition, to play a role on limiting the level of specific energy, particle crushing has other impact on the model, albeit minor. One notable point is that with the inclusion of particle crushing is that failure progression is smoother. Figure 3.38(a) shows a case where even though there was a shallow cut, without particle crushing, an extended horizontal crack was developed. However, under the same numerical setup conditions, but with the inclusion of particle crushing, the damage observed in front of the cutter mimics the ductile failure mode as is shown in Figure 3.38 (b), and the macro-cracks are formed towards the bulk of the material.

(a)   **(b)**
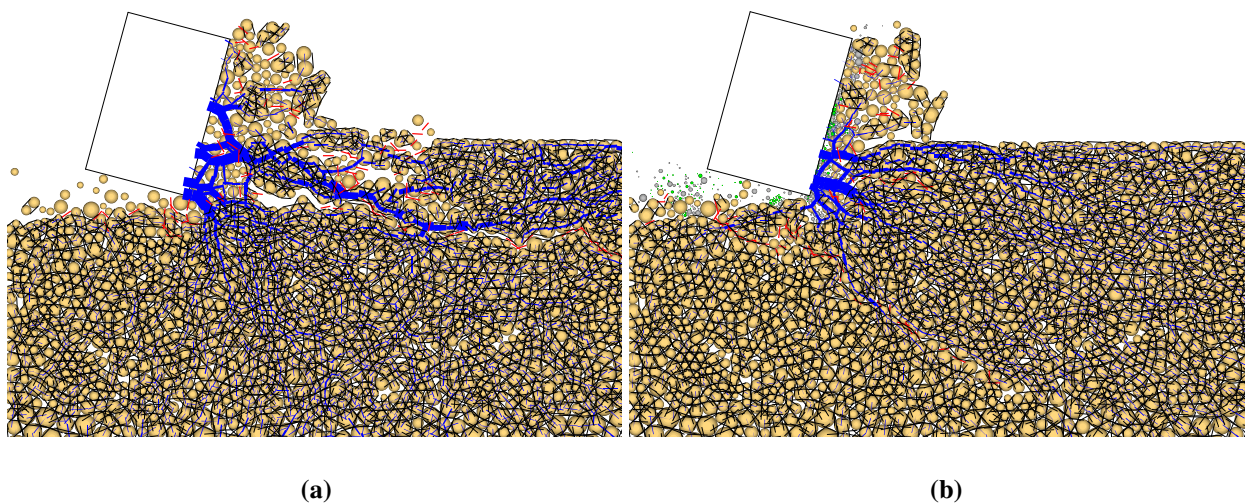
Figure 3.38 Impact of particle crushing on failure configuration when (a) crushing is not consider, and (b) when crushing is implemented

The other point of interest is that particle crushing affects the specimen configuration behind the cutter. Figure 3.39 depicts the final configuration of a RST in the two strongest materials in CASE I, and encircled it can be observed that the failure with respect to crack propagation in the strongest material is less, or does not exist in some areas. Thus the strength of the bonds is not being considered in the failure mechanical response of the scratching.

SS_75_I

(a)
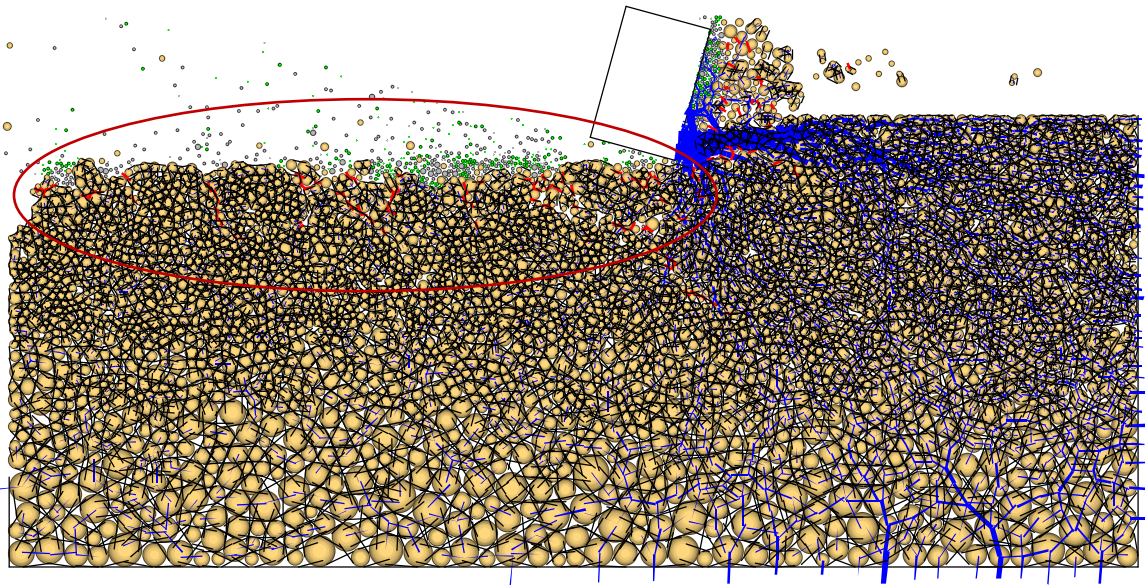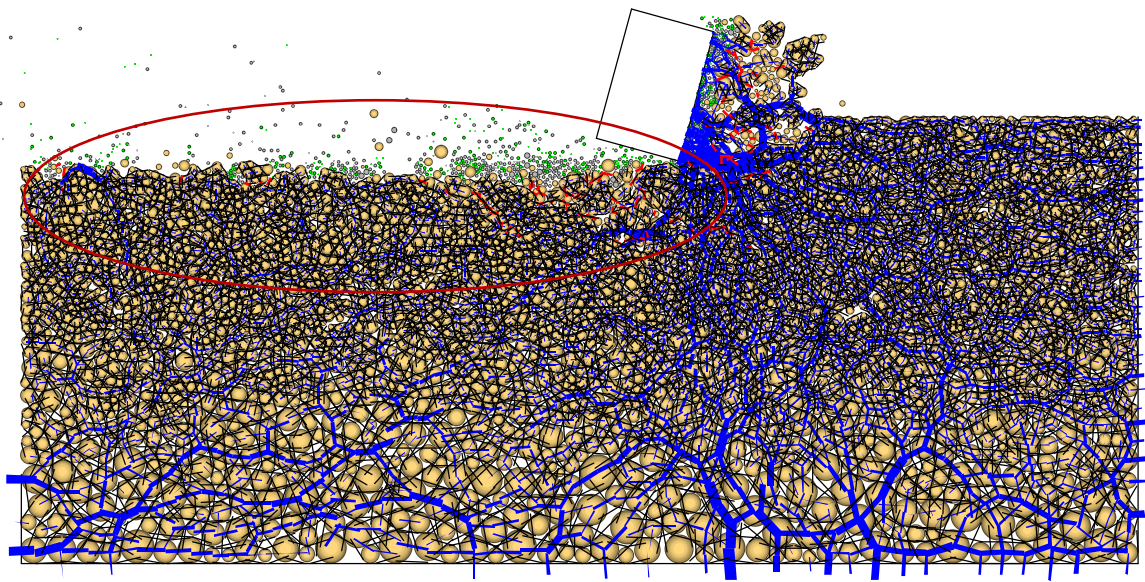
SS_100_I

(b)

Figure 3.39 Failure characteristics affected by particle crushing strength in (a) *SS_75_I* and (b) *SS_100_I*

4.0   CONCLUSIONS

This research has demonstrated that DEM is capable of modeling rock cutting as represented by the linear scratching test. DEM procedure, as laid out in this study, not only is capable of reproducing the rock fragmentation process induced by a PDC bit, but it is also capable to obtain cutter forces quantitatively that are compatible to those from physical tests. Most convincing of all, on the quantitative nature of the results, is that this study was able to reproduce an important relationship between the cutter specific energy input and the rock strength. We have also found that failure mode cannot be dictated by the depth of cut. The velocity of cutting also plays a role. As the study demonstrates, at least computationally, that a slow cutting velocity may force a shallow cut into a brittle failure while a faster cutting process gives a ductile failure at same cutting depth.

When trying to model a physical test, one uncertain factor in an analysis has been the selection of cutting velocity. It is not possible to employ the actual velocity of the cutter from that of a physical test. At the present time, a sensitivity study is suggested so that a proper cutting velocity can be selected for numerical modeling that reproduces observation expected of a physical test.

This study also found that particle crushing has a significant impact on the RST results. Although with uncertainty on the crushing strength of fine particles, the inclusion of particle crushing in the modeling gave a better representation of failure modes. From the cutting force

perspective, the crushing of particles does not seem to affect the resulting cutting forces unless the strength of the rock is very high. This study predicts that the cutter force has an upper bound that is dictated by the rock strength. Because the lacking of crushing strength data on small particles, the predicted bounds are given a range.

With the present work, demonstrating the feasibility of numerical modeling of linear RST, future research of modeling circular cutting action similar to that of oil drilling using 3D DEM is in order that may have impact on industrial applications particularly in the area of oil drilling.

Finally, in terms of linear RST modeling, more research on modeling deeper cuts is also needed. As for nature of rock modeling, research on general DEM micro-parameter estimation is also a worthwhile undertaking.

BIBLIOGRAPHY

[1]   Richard T, Detournay E, Drescher A, Nicodeme O and Fourmaintraux D. The scratch test as a means to measure strength of sedimentary rocks. In: SPE/ISRM Rock Mechanics in Petroleum Eng. Conference, Trondheim, Norway, 1998. 15-22.

[2]   Cundall PA and Strack ODL. A discrete numerical model for granular assemblies. Géotechnique, 1979; 29: 47-65.

[3]   Richard T, Determination of strength from cutting tests. 1999, University of Minnesota: Minneapolis, MN. p. 99.

[4]   Cundall PA. A computer model for simulating progressive large scale movements in blocky rock systems. In: Proceedings of the Symposium of the International Society of Rock Mechanics, Nancy, France, 1971.

[5]   Potyondy DO and Cundall P. A bonded-particle model for rock. International Journal of Rock Mechanics and Mining Sciences, 2004; 49: 1329-64.

[6]   Itasca Consulting Group Inc. PFC2D/3D (Particle Flow Code in 2/3 Dimensions), Version 4.0. Minneapolis, MN: ICG; 2008.

[7]   Detournay E and Defourny P. A Phenomenological Model for the Drilling Action of Drag Bits. International Journal of Rock Mechanics and Mining Sciences, 1992; 29: 13-23.

[8]   Schei G, Fjaer E, Detournay E, Kenter CJ, Fuh GF and Zausa F. The scratch test: An Attractive technique for determining strength and elastic properties of sedimentary rocks. In: SPE Annual Technical Conference and Exhibition, Dallas, Texas, 2000.

[9]   Huang H, Detournay E and Bellier B. Discrete element modeling of rock cutting. In: The 37th U.S. Rock Mechanics Symposium. Rock Mechanics for Industry, Vail, USA, 1999. 123-30.

[10]   Lei ST and Kaitkay P. Distinct Element Modeling of Rock Cutting under Hydrostatic Pressure. Key Engineering Materials, 2003; 250: 110-17.

[11] Lei ST, Kaitkay P and Shen X, Simulation of rock cutting using distinct element method - PFC^{2D}, In: Numerical Modeling in Micromechanics Via Particle Methods. Leiden: A.A. Balkema Publishers, pp.63-71.

[12] Rojek J. Discrete element modeling of rock cutting. Computer Methods in Materials Science, 2007; 7: 224-30.

[13] Nishimatsu Y. The mechanics of rock cutting. International Journal of Rock Mechanics and Mining Sciences & Geomechanics Abstracts, 1972; 9: 261-70.

[14] Evans I. The force requiered for pointed attacks picks. International Journal of Mining Engineering, 1965; 2: 63-71.

[15] Huang H and Detournay E. Intrinsic Length Scales in Tool-Rock Interaction. International Journal of Geomechanics, 2008; 8: 39-44.

[16] Block G and Jin H. Role of failure mode on rock cutting dynamics. In: SPE Annual Technical and Exhibition, New Orleans, Louisiana, 2009.

[17] Deere DU and Miller RP, Engineering classification and index properties for intact rock. 1966, Air Force Weapons Lab: Kirtland Air Base, New Mexico.

[18] Bell FG. Engineering Properties of Soils and Rocks. London: Blackwell Science Ltd., 2000.

[19] McDowell GR and Amon A. The application of Weibull statistics to the fracture of soil particles. Soils and Foundations, 2000; 40: 133-41.

[20] Tsuongui O, Vallet D and Charmet J-C. Numerical model of crushing of grains inside two-dimensional granular materials. Powder Technology, 1999; 105: 190-98.

[21] Åström JA and Herrmann HJ. Fragmentation of grains in a two-dimensional packing. The European Physical Journal B, 1998; 5: 551-54.

[22] Bathurst RJ and L. R. Micromechanical aspects of isotropic granular assemblies with linear contact interactions. Journal of Applied Mechanics, 1988; 55: 17-23.

[23] McDowell GR and Bolton MD. On the micromechanics of crushable aggregates. Géotechnique, 1998; 48: 667-79.

[24] Nakata Y, Hyde AFL, Hyodo M and Murata H. A probabilistic approach to sand particle crushing in the triaxial test. Géotechnique, 1999; 49: 567-83.

[25] Nakata Y, Kato Y, Hyodo M, Hyde AFL and Murata H. One-dimensional compression behaviour of uniformly graded sand related to single particle crushing strength. Soils and Foundations, 2001; 41: 39-51.

[26] McDowell GR. Statistics of soil particle strength. Géotechnique, 2001; 51: 897-900.

[27]   Antonyuk S, Tomas J, Heinrich S and Lothar M. Breakage behaviour of spherical granulates by compression. Chemical Engineering Science, 2005; 60: 4031-44.

[28]   Tan Y, Yang D and Sheng Y. Discrete Element Method (DEM) modeling of fracture and damage in the machining process of polycristalline SiC. Journal of the European Ceramic Society, 2009; 29: 1029-37.

[29]   Dagrain F and Richard T, On the influence of PDC wear and rock type on friction coeffictient and cutting efficiency, in EUROROCK 2006: Multiphysics coupling and long term behaviour in rock mechanics, A Van Cotthen, et al., Editors. 2006, Taylor and Francis Group: Liège, Belgium.

[30]   Bésuelle P, Desrues J and Raynaud S. Experimental characterisation of the localisation phenomenon inside a Vosges sandstone in a triaxial cell. International Journal of Rock Mechanics and Mining Sciences, 2000; 37: 1223-37.